Detection of nitroaromatic vapours with diketopyrrolopyrrole thin films: exploring the role of structural order and morphology on thin film properties and fluorescence quenching efficiency

Article

Supplemental Material

Supplementary Information

Detection of nitroaromatic vapours with diketopyrrolopyrrole thin films: Exploring the role of structural order and morphology on thin film properties and fluorescence quenching efficiency

Monika Warzecha,[a] Jesus Calvo-Castro,[a] Alan R. Kennedy,[b] Alisdair Macpherson,[c] Kenneth Shankland,[d] Norman Shankland,[e] Andrew J. McLean[a*] and Callum J. McHugh[a*]

[a] School of Science, University of the West of Scotland, Paisley, UK; Fax: +44 141 848 3204; Tel: +44 141 848 3210; E-mail: callum.mchugh@uws.ac.uk
[b] Department of Pure and Applied Chemistry, University of Strathclyde, Glasgow, UK
[c] Photon Science Institute, University of Manchester, Manchester, UK
[d] School of Pharmacy, University of Reading, Reading, UK.
[e] Crystallografx Ltd. Milngavie, Glasgow, UK.

SI.1. Preparation of HBDPP and BBDPP

Reagents and instrumentation: **HBDPP** and **BrBDPP** were prepared according to the literature methods described previously.[1] **BBDPP** was prepared using a modified version of the method described previously[2]. Unless otherwise stated, all starting materials and reagents were obtained from Sigma Aldrich and used as received. ^{1}H NMR and ^{13}C NMR spectra were determined using a JEOL ECS400 400 MHz spectrometer (in CDCl$_3$). Elemental analyses were carried out using the service provided at Jagiellonian University in Krakow, Poland. FTIR analyses were carried out on the neat samples by attenuated total reflectance using a Perkin Elmer, Spectrum One FTIR Spectrometer, with Universal ATR Sampling Accessory.

Synthesis:

2,5-Dibenzyl-3,6-diphenylpyrrolo[3,4-c]pyrrole-1,4(2H,5H)-dione **(HBDPP)**[1]. ^{1}H NMR (CDCl$_3$): 4.95 (4H, s, CH$_2$), 7.18 (4H, d, ArH), 7.23-7.30 (6H, m, ArH), 7.41-7.46 (6H, m, ArH), 7.73(4H, d, ArH). 13C NMR (CDCl$_3$): 46.0 (CH$_2$), 126.8 (C=C) 127.5 (C=C), 127.9 (C=C), 128.8 (C=C), 128.9 (C=C), 129.1 (C=C), 131.5 (C=C), 137.5 (C=C), 149.1 (C=C), 163.2 (C=O). IR (ATR)/cm^{-1}: 3033 (ArH), 2932 (CH$_2$), 1659 (C=O), 1603 (C=C), 1566 (C=C), 1496 (C=C), 1382 (CH$_2$), 1358 (CH$_2$), 728 (ArH). Anal. Calcd for C$_{32}$H$_{24}$N$_2$O$_2$: C, 82.03; H, 5.16; N, 5.98. Found: C, 81.77; H, 5.21; N, 5.76. Melting point: 278 °C.

2,5-Dibenzyl-3,6-bis(4-bromophenyl)pyrrolo[3,4-c]pyrrole-1,4(2H,5H)-dione **(BrBDPP)**[1]. ^{1}H NMR (CDCl$_3$): 4.94 (4H, s, CH$_2$), 7.16 (4H, d, ArH), 7.24 – 7.30 (6H, m, ArH), 7.56 (4H, d, ArH), 7.63 (4H, d, ArH).^{13}C NMR (CDCl$_3$): 45.8 (CH$_2$), 126.3 (C=C), 126.7 (C=C), 127.7 (C=C), 129.0 (C=C), 130.6 (C=C), 132.3 (C=C), 137.2 (C=C), 148.2 (C=C), 162.7 (C=O). IR (ATR)/cm^{-1}: 3031 (ArH), 2990 (CH$_2$), 1658 (C=O), 1586 (C=C), 1542 (C=C), 1377 (CH$_2$), 1354 (CH$_2$), 834 (ArH), 823 (ArH), 695 (ArH), 683 (ArH). Anal. Calcd for C$_{32}$H$_{22}$N$_2$O$_2$Br$_2$: C, 61.36; H, 3.54; N, 4.47. Found: C, 61.53; H, 3.56; N, 4.58. Melting point: 250 °C.

2,5-Dibenzyl-3,6-bis(4'-butoxy-[1,1'-biphenyl]-4-yl)pyrrolo[3,4-c]pyrrole-1,4(2H,5H)-dione **(BBDPP)**[2]. A mixture of Pd(OAc)$_2$ (1.00 mg, 0.004 mmol), SPhos (3.20 mg, 0.008 mmol), 4-butoxyphenyl boronic acid (43.80 mg, 0.225 mmol), **BrBDPP** (41.10 mg, 0.065 mmol) and K$_3$PO$_4$ (62.7 mg, 0.297 mmol) in THF (3.70 ml) was stirred for 23 h at 60 °C under nitrogen atmosphere. After evaporation of the solvent purification of the remaining residue by wet

chromatographic column eluting with DCM gave **BBDPP** as a bright red powder (33.29 mg, 67 %). ^{1}H NMR (CDCl$_3$): 0.98 (6H, t, CH$_3$), 1.45-1.55 (4H, m, CH$_2$), 1.78 (4H, q, CH$_2$), 3.99 (4H, t, CH$_2$), 5.05 (4H, s, CH$_2$), 6.97 (4H, d, ArH), 7.23-7.34 (10H, m, ArH), 7.54 (4H, d, ArH), 7.63 (4H, d, ArH), 7.85 (4H , d, ArH). ^{13}C NMR (CDCl$_3$) 14.0 (CH$_3$), 19.3 (CH$_2$), 31.4 (CH$_2$), 45.9 (CH$_2$), 67.9 (CH$_2$), 109.7 (C=C), 115.0 (C=C), 126.0 (C=C), 126.7 (C=C), 126.9 (C=C), 127.5 (C=C), 128.3 (C=C), 128.9 (C=C), 129.7 (C=C), 132.1 (C=C), 137.7 (C=C), 143.8 (C=C), 148.7 (C=C), 159.5 (C=C), 163.0 (C=O). IR (ATR)/cm^{-1}: 3035 (ArH), 2950, 2927, 2868 (CH$_2$ & CH$_3$), 1670 (C=O), 1595 (C=C), 1495 (C=C), 1451 (CH$_3$), 822 (ArH), 734 (ArH), 719 (ArH); *Anal. Calcd for C$_{52}$H$_{48}$N$_2$O$_4$*: C, 81.65; H, 6.32; N, 3.66. *Found:* C, 81.04; H, 6.12; N, 3.58. Melting Point: 266 °C.

SI.2. Single Crystal Structure Determination of BBDPP

Crystal data for compound BBDPP: The single crystal of **BBDPP** was obtained by slow evaporation of a $CHCl_3$ solution. Data were measured by the National Crystallography Service with a sealed tube Rigaku instrument.[3] Refinement was to convergence against F^2 and used the program SHELXL-97.[4] Final parameters; $C_{52}H_{48}N_2O_4$, $M_r = 764.92$, monoclinic, space group P2$_1$/n, $a = 20.5116(14)$, $b = 5.1146(4)$, $c = 21.4898(15)$ Å, $\beta = 116.490(2)$ °, $V = 2017.8(3)$ Å^3, $Z = 2$, $\lambda = 0.71075$ Å, $\mu = 0.079$ mm^{-1}, $T = 100(2)$ K; 20043 reflections, 4616 unique, $R_{int} = 0.0807$; $R = 0.0486$ (F, 3144 obs. data only) and $R_w = 0.1222$ (F^2, all data), GOF = 1.022.

CCDC reference number **CCDC-1019568**. See http://www.rsc.org/suppdata/cc for full crystallographic data in CIF or other electronic format.
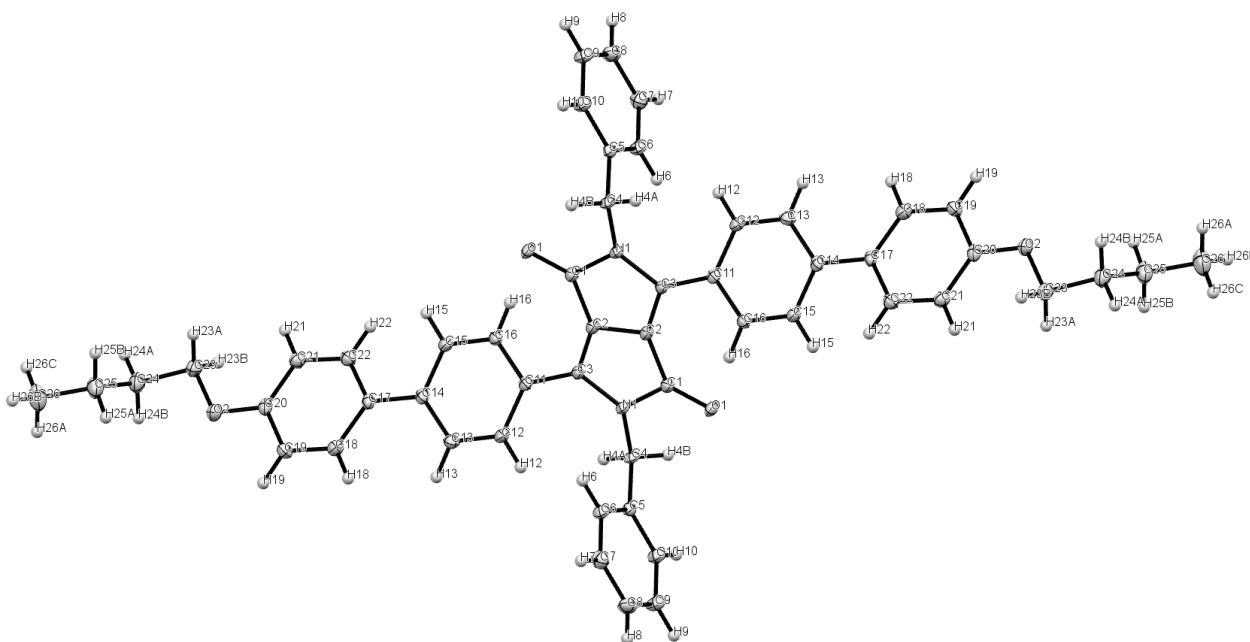

Fig. S2.1. Molecular structure of **BBDPP** as determined by single crystal diffraction. Atom labels are as shown.
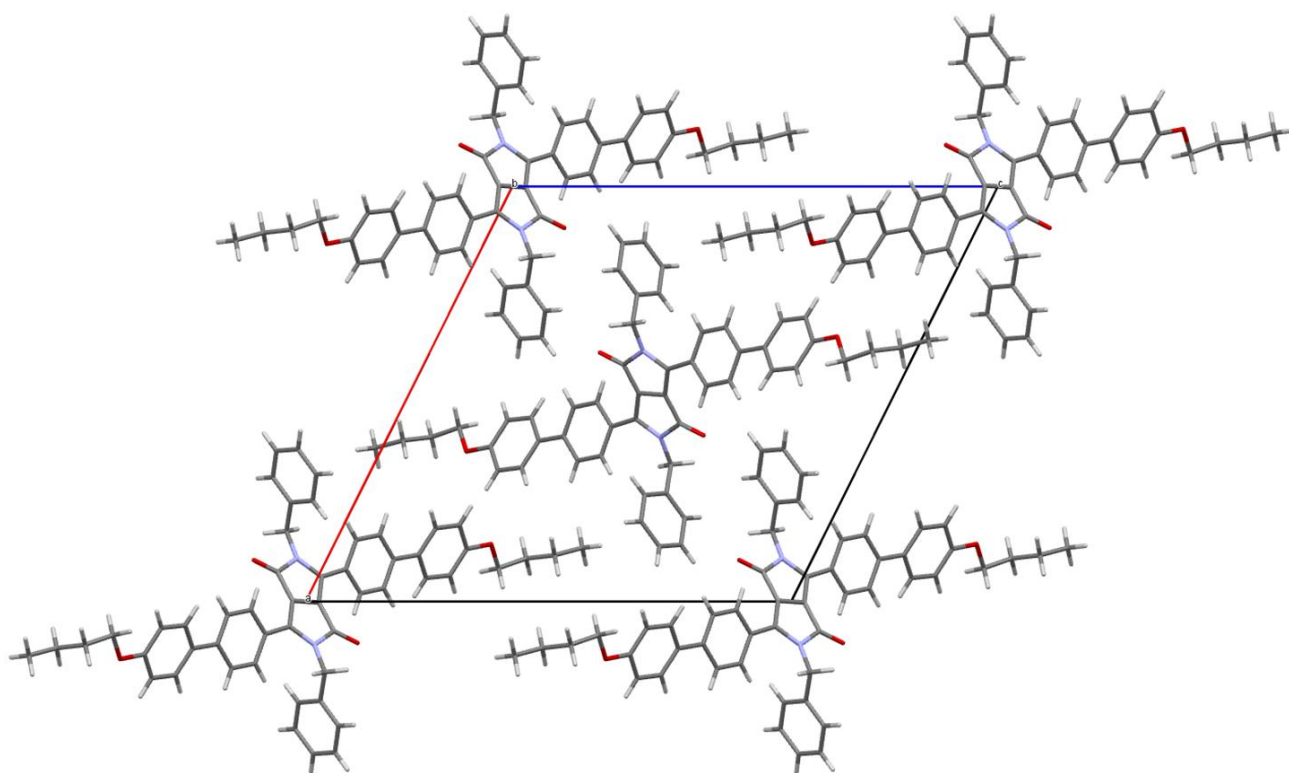
Fig. S2.2. Single crystal structure of **BBDPP** (unit cell view).
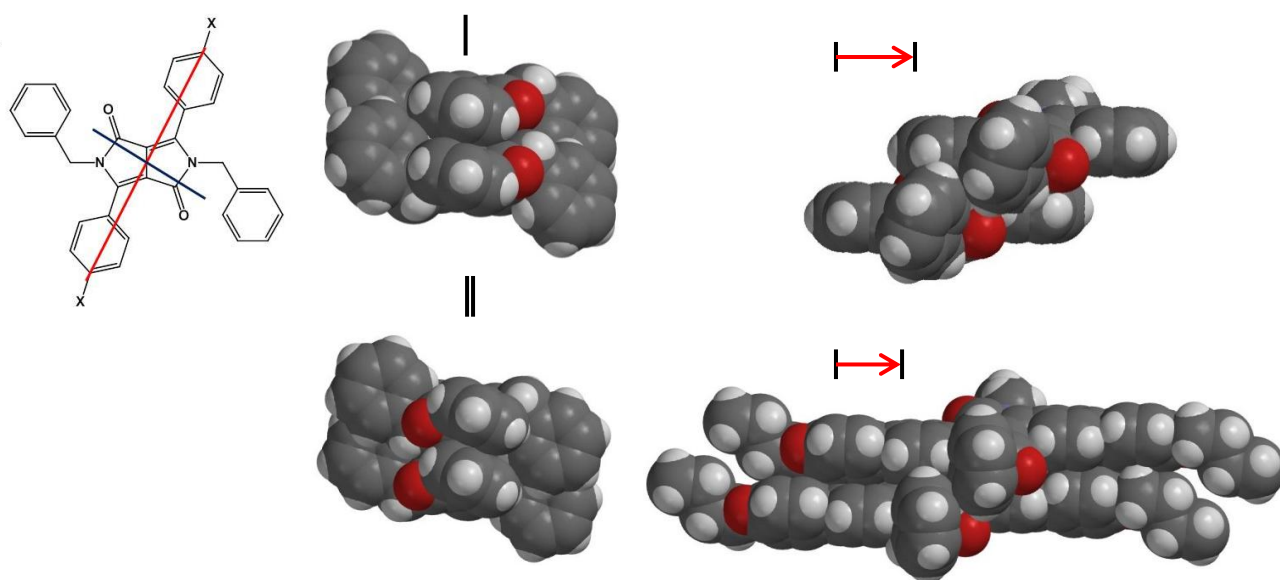

Fig. S2.3. Space filled representations of **HBDPP** (top) and **BBDPP** (bottom) single crystal structures determined with short and long molecular axes in blue and red respectively (molecular structure, top left). The long and short molecular axis perspective views of the crystal extracted π-π overlapped dimers are shown for both structures (left and right columns respectively).[1]

SI.3. Optical and Electrochemical Characterisation

Optical Spectroscopy and Photophysics: HPLC grade dichloromethane was purchased from Fischer-Scientific and used as supplied. Absorption spectra of solutions and thin films were recorded using a Perkin-Elmer Lambda 40 UV/Vis spectrophotometer. Unless otherwise stated, thin film absorption spectra were corrected for scattering. In short, a part of the spectrum was selected where the absorbance was caused only by scatter. A polynomial was then fitted to this part of the spectrum using a least-squares fit to the logarithm of the absorbance. Using the coefficients determined from the fit, the scatter contributions at all other wavelengths were calculated and then subtracted from the measured spectrum to leave the absorbance of the film. Reflectance spectra of solid powders were obtained using a Perkin-Elmer Lambda 9 UV/Vis spectrometer equipped with a Perkin-Elmer integrating sphere attachment and converted to absorption spectra using the Kubelka-Munk function. Emission spectra were collected in right angle mode for solutions and front face mode for solids and thin films using a Perkin-Elmer LS50b luminescence spectrometer equipped with Hamamatsu R928 photomultiplier tube (185 to 900 nm). Fluorescence emission spectra shown were corrected for the photomultiplier response using the manufacturer correction method. Fluorescence quantum yields in solution were determined from the area of the corrected fluorescence spectra with reference to Rhodamine 6G in ethanol (ϕ_F = 0.95 at 490nm excitation wavelength)[5] using the method of Parker and Rees.[6] A correction was applied to take into account the refractive index differences between dichloromethane and ethanol. Rhodamine 6G (99 %) was purchased from Acros Organics and used as supplied without any further purification. Absorption spectra of **HBDPP** and **BBDPP** were measured with an optical density of < 0.08 for the highest concentration employed. Samples were degassed prior to any measurement with oxygen-free nitrogen gas (BOC) for 10 min. Absorption spectra were recorded before and after degassing to account for any possible changes in concentration resulting from evaporation of the solvent. Fluorescence lifetimes of **HBDPP** and **BBDPP** were measured in dichloromethane solution using an apparatus based upon a Mai Tai HP laser purchased from Newport Spectra-Physics with a < 100 fs pulse width and a tuning range of 690 - 1040 nm. The < 1.2 mm beam from the latter was pulse-picked using an APE PulseSelect to reduce the initial repetition rate of 80±1 MHz by a factor of x20. A small fraction of the beam was picked off with a beam sampler to trigger an amplified fast-start photodiode OT-900 purchased from Edinburgh Instruments. This beam

sampler consisted of a wedged plate to split off ~4% of the beam to provide a start synchronization pulse. The main part of the laser beam was sent to a HarmoniXX harmonic generator purchased from APE GmbH to double the frequency of the beam to that of the desired excitation wavelength. The laser beam was then routed via steering mirrors and a periscope to the sample cuvette via a Berek's compensator. The emission light was collected and focused onto the slits of a Horiba Spex 1870C 0.5m monochromator after filtering and passed through a polarizing film set at the magic angle. The emission was detected with a TE-cooled Hamamatsu R3809U-50 microchannel plate-photomultiplier tube (MCP-PMT) operating at -3kV (Edinburgh Instruments housing, MCP cooler power supply and HV power supply). The amplified output (Becker & Hickl HFAC-26dB) from the MCP-PMT and fast photodiode were sent to a TCC900 supplied by Edinburgh Instruments for TCSPC and signal processing. Datasets obtained for **HBDPP** and **BBDPP** recorded using 470 nm excitation and emission wavelengths between 530 nm and 640 nm were fit to single exponential decays by least square iterative re-convolution with the approx. 90 ps instrument response function.

Table S3.1. Absorption (λ_{abs}) and fluorescence emission maxima (λ_{em}), molar absorptivity (ε), fluorescence quantum yield (Φ_F) and excited state lifetimes (τ_0) of **HBDPP** and **BBDPP** in dichloromethane solution.

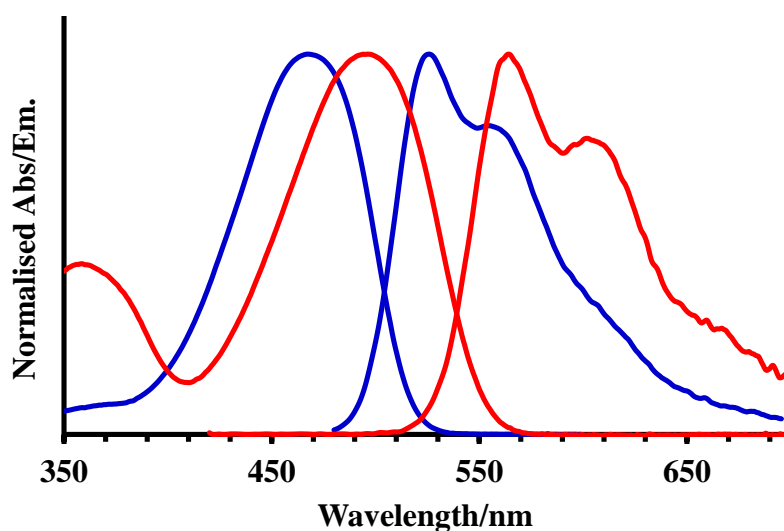|	λ_{abs} (nm)	λ_{em} (nm)	ε ($M^{-1}cm^{-1}$)	Φ_F	τ_0 (ns)	E_{0-0} (cm^{-1})	Stokes Shift (cm^{-1})
HBDPP	464	524	13580	0.85	6.46	19865	2467
BBDPP	492	561	34880	0.81	3.95	18639	2499

Figure S3.1. Normalised **HBDPP** (blue) and **BBDPP** (red) absorption and emission (Ex. 450 nm & 490 nm respectively) spectra in dichloromethane solution.

Table S3.2. Absorption (λ_{abs}) and fluorescence emission maxima (λ_{em}) for **HBDPP** powder and *as-deposited* spin-coated thin films on SiO_2.

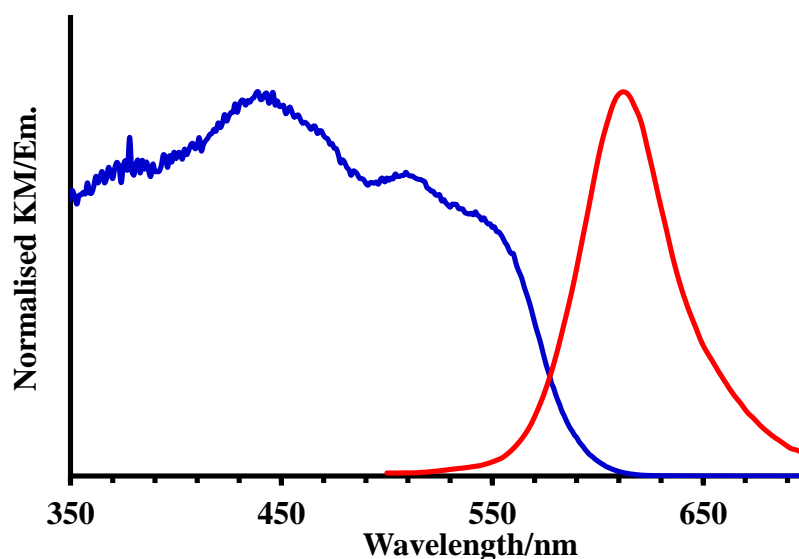|	**Powder**	**Amorphous thin film**	*As-deposited* **ordered thin film**
λ_{abs} **(nm)**	439	473	481, 507
λ_{em}**(nm)**	612	530, 563	537, 565
E_{0-0} **(cm^{-1})**	-	19474	19120
Stokes Shift (cm^{-1})	-	2273	1101

Figure S3.2. Normalised Kubelka-Munk derived absorption and emission (Ex. 450 nm) spectra of **HBDPP** powder.
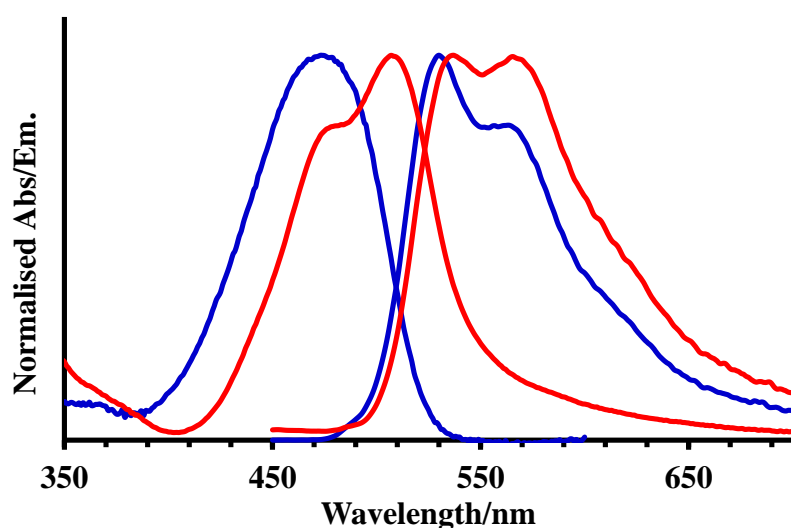

Figure S3.3. Normalised absorption and emission (Ex. 430 nm) spectra from a 180 nm thick amorphous (blue) and 230 nm thick *as-deposited* ordered (red) **HBDPP** thin film.

Table S3.3. Absorption (λ_{abs}) and fluorescence emission maxima (λ_{em}) for **BBDPP** powder and *as-deposited* spin coated thin films on SiO_2.

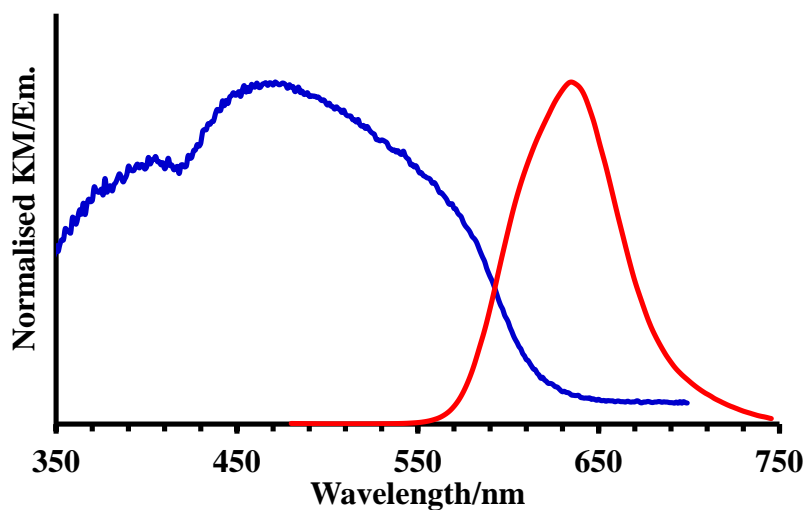|	**Powder**	**Amorphous thin film**	***As-deposited* ordered thin film**
λ_{abs} **(nm)**	471	516	535, 561
λ_{em} **/ (nm)**	635	597, 628	597, 643
$E_{0\text{-}0}$ **(cm^{-1})**	-	17809	17064
Stokes Shift (cm^{-1})	-	2629	1074

Figure S3.4. Normalised Kubelka-Munk derived absorption and emission (Ex. 490 nm) spectra of **BBDPP** powder.
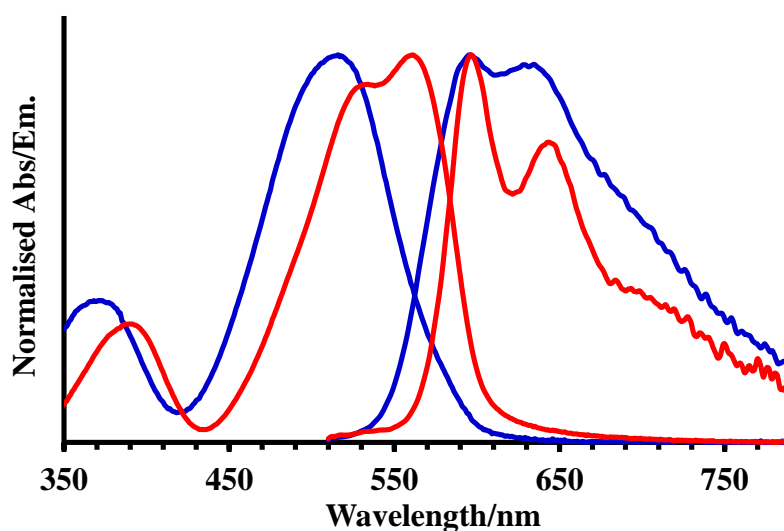

Figure S3.5. Normalised absorption and emission (Ex. 490 nm) spectra from a 210 nm thick amorphous (blue) and 245 nm thick *as-deposited* ordered (red) **BBDPP** thin film.
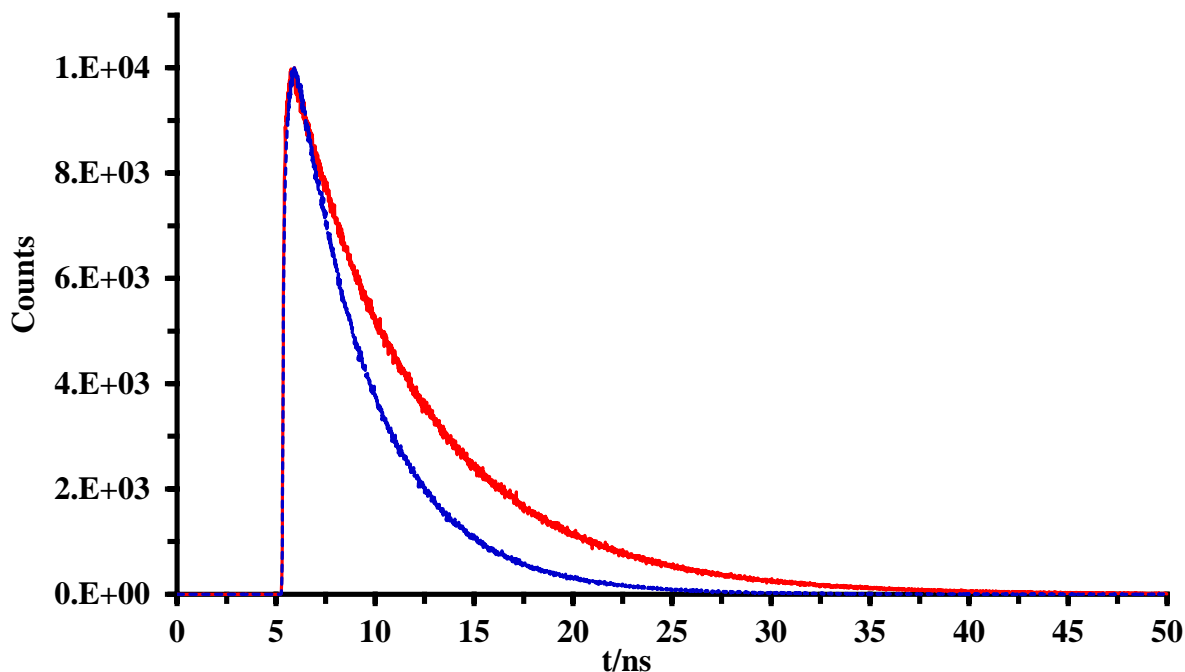
Figure S3.6. Time resolved excited state decay of **HBDPP** (red) and **BBDPP** (blue) in dichloromethane solution.

Electrochemical Analysis: Electrochemical measurements were performed by cyclic voltammetry using a Metrohm Autolab PGSTAT30 potentiostat. A conventional three-electrode configuration was employed with glassy carbon working electrode (BAS Inc.), platinum wire auxiliary electrode (BAS Inc.) and Ag/AgCl (0.1 M NaCl) reference electrode (BAS Inc.). The glassy carbon electrode and platinum working electrode were electrochemically cleaned before and after each measurement using a 0.5 M sulphuric acid solution by running oxidative scans at 0.05 V s^{-1} and 0.1 V s^{-1} respectively. In addition, the surface of the glassy carbon electrode was polished prior to any measurement utilising the manufacturer provided cleaning kit. Ferrocene was employed as internal standard reference and tetrabutylammonium hexafluorophosphate (98%, Sigma-Aldrich) as supportive electrolyte at a concentration of 0.1 M in dichloromethane. The concentrations of **HBDPP**, **BBDPP**, **NB**, **DNT** and **TNT** were set to 10^{-3} M in dichloromethane and all measurements were conducted under dry argon (BOC) by outgassing the voltammetry cells for 10 min. Molecular modelling studies were carried out using the indicated density functionals and basis sets, as implemented in Spartan10 software.[7]

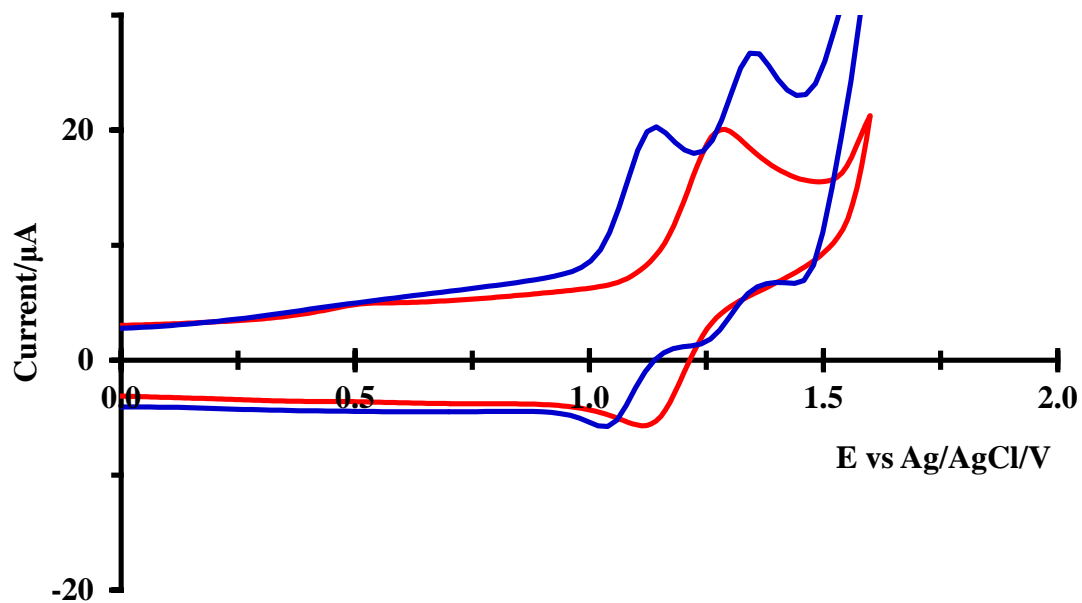**Figure S3.7.** Oxidation CVs for **HBDPP** (red line) and **BBDPP** (blue line) in dichloromethane at 100 mVs^{-1} scan rate.
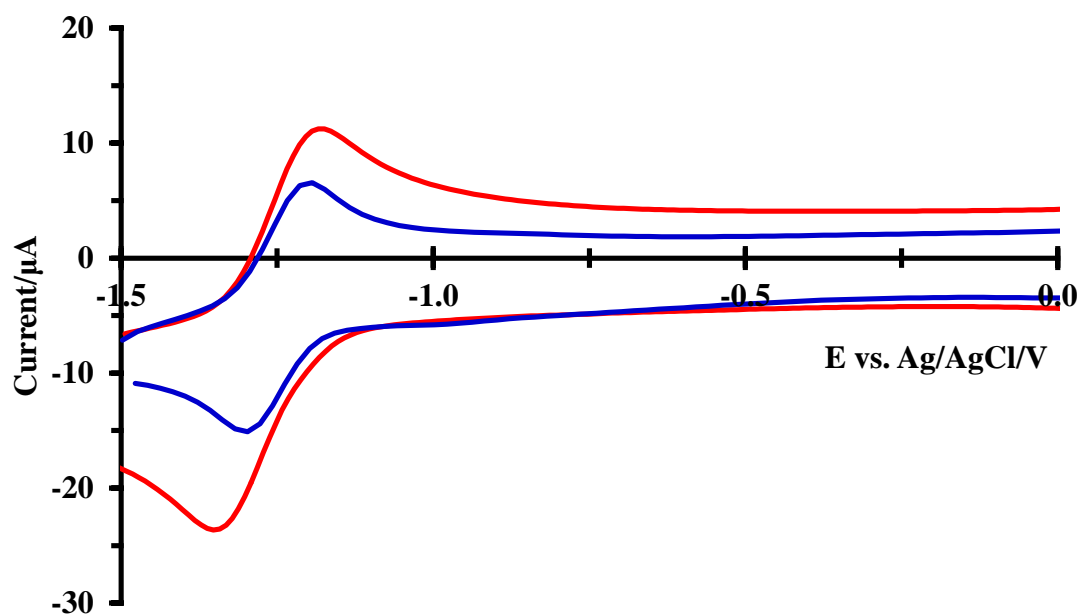
Figure S3.8. Reduction CVs for **HBDPP** (red) and **BBDPP** (blue) in dichloromethane at 100 mVs^{-1} scan rate.

Figure S3.9. Oxidation and reduction CVs for **NB** (green), **DNT** (blue) and **TNT** (red) in dichloromethane at 100 mV s^{-1} sca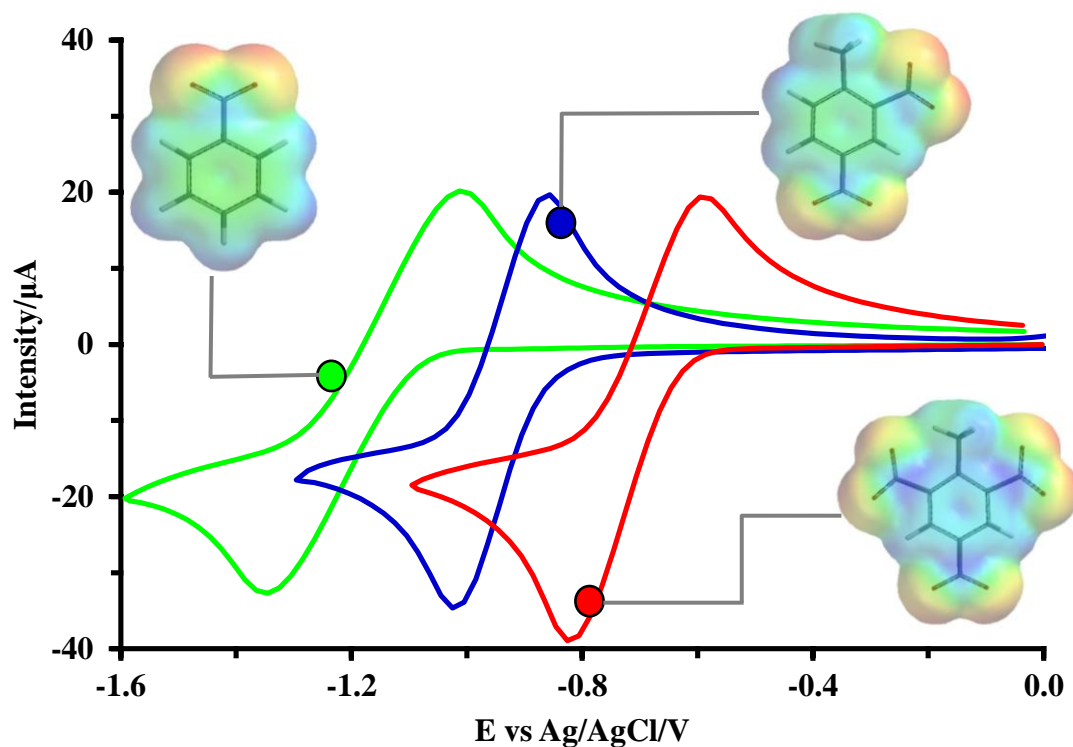n rate. Insets illustrate the electrostatic potential maps for the neutral optimized geometries of the nitroaromatics at M06-2X/6-31G(d).
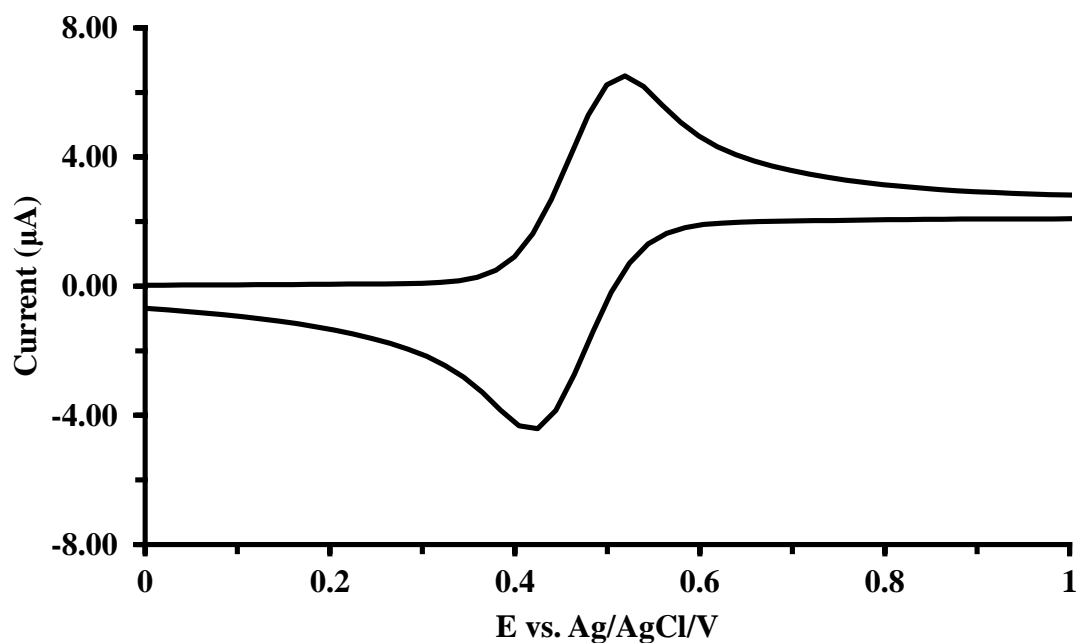

Figure S3.10. Oxidation and Reduction CVs of Ferrocene in dichloromethane at 100 mV s^{-1} scan rate.

Table S3.4. Cathodic and anodic peak positions, E_{pc} and E_{pa}, peak separation, ΔE_p, and half-wave potentials, $E_{1/2}$, for the oxidation and reduction of **HBDPP**, **BBDPP** and the reduction of **NB**, **DNT** and **TNT** in dichloromethane at 100 mV s^{-1} scan rate. $E_{1/2}$ vs. Ag/AgCl in 0.1M NBu$_4$PF$_6$.

Compound	Oxidation				Reduction			
	E_{pc} (V)	E_{pa} (V)	ΔE_p (V)	$E_{1/2}$ (V)	E_{pc} (V)	E_{pa} (V)	ΔE_p (V)	$E_{1/2}$ (V)
HBDPP	1.132	1.280	0.148	1.210	-1.342	-1.184	0.158	-1.260
BBDPP	1.039	1.123	0.084	1.080	-1.297	-1.194	0.103	-1.250
NB	-	-	-	-	-1.325	-1.013	0.312	-1.169
DNT	-	-	-	-	-1.025	-0.856	0.169	-0.941
TNT	-	-	-	-	-0.806	-0.596	0.201	-0.701

HOMO and LUMO energy level determination: The HOMO and LUMO energies of **HBDPP** and **BBDPP** and the LUMO energies of NB, DNT, and TNT were estimated utilising their determined oxidation and reductions potentials vs. SCE through the application of Equations S3.1. and S3.2. employing the oxidation onset for Ferrocene, ($E_{1/2}^{Fc}$ = -0.517 V vs. SCE) as standard.[8-10] The E_{HOMO} for Ferrocene was taken as -4.8 eV.[11]

$$E_{HOMO} = -\left[\left(E_{1/2}^{ox} - E_{1/2}^{Fc}\right) + 4.8\right] \qquad \textbf{Equation S3.1.}$$

$$E_{LUMO} = -\left[\left(E_{1/2}^{red} - E_{1/2}^{Fc}\right) + 4.8\right] \qquad \textbf{Equation S3.2.}$$

Table S3.5. Experimentally determined oxidation, $E_{1/2}^{ox}$ and reduction, $E_{1/2}^{red}$ onsets for **HBDPP** and **BBDPP** and $E_{1/2}^{red}$ onsets for **NB**, **DNT** and **TNT** in dichloromethane vs. SCE and their associated HOMO and LUMO energies.

Compound	$E_{1/2}^{ox}$ / V	E_{HOMO} / eV	$E_{1/2}^{red}$ / V	E_{LUMO} / eV
HBDPP	1.245	-5.528	-1.186	-3.097
BBDPP	1.126	-5.409	-1.165	-3.118
NB	-	-	-1.116	-3.167
DNT	-	-	-0.901	-3.382
TNT	-	-	-0.657	-3.626

SI.4. Solution Based Steady State Fluorescence Quenching

Stern-Volmer analysis: Steady state fluorescence quenching experiments of **HBDPP** and **BBDPP** were carried out in HPLC grade dichloromethane. The quenchers, **NB** (99 %) and **DNT** (97 %), were purchased from Acros Organics and Sigma-Aldrich respectively and used without further purification. Small quantities of **TNT** were obtained from the University of Strathclyde and used as received in solution. Stern-Volmer experiments were performed employing no less than 5 aliquots of each quencher with increasing concentration, whilst maintaining a constant fluorophore concentration for both **HBDPP** and **BBDPP**. Solution absorbance was measured pre and post quencher addition in order that fluorescence intensity could be corrected for the possibly of variation in absolute photon absorption and the presence of ground state complexes could be investigated at high quencher concentration. Good linearity and intercepts were obtained for all the DPP/quencher combinations investigated and no evidence of inner-filter effect was observed. From the resulting Stern-Volmer plots the Stern-Volmer constants, K_{sv} were extracted from the slope of the straight line and employed with the fluorophore lifetimes, τ_0 to determine the bimolecular rate constants, k_q, which were compared to the estimated theoretical diffusion controlled rate limits, k_d in each case. Values of k_d were determined using the Smoluchowski[12] expression denoted in Equation S4.1,

$$k_d = \frac{4\pi N_A}{1000} \cdot \left(R_{DPP} + R_Q\right) \cdot \left[\frac{k_B T}{6\pi\eta} \cdot \left(\frac{1}{R_{DPP}} + \frac{1}{R_Q}\right)\right] \qquad \textbf{Equation S4.1.}$$

where N_A and η denote Avogadro's number and viscosity of the solvent. The radii for **HBDPP** and **BBDPP** and the quenchers employed are represented by R_{DPP} and R_Q respectively and were obtained from the van der Waals molecular volumes from optimised geometries of these systems employing M06-2X/6-31G(d). In addition, the driving force for electron transfer was estimated by determination of the Gibbs free energy, ΔG which was calculated for **HBDPP** and **BBDPP** utilising Equation S4.2 and electrochemical data reported in SI.3:

$$\Delta G = E^{\circ}(D^+/D) - E^{\circ}(A/A^-) - \Delta E_{0,0} \qquad \textbf{Equation S4.2.}$$

14

where $E^°(D^+/D)$ was the oxidation potential of **HBDPP** and **BBDPP** and $E^°(A/A^-)$ was the reduction potential of the nitroaromatic (with the negative sign). $\Delta E_{0,0}$ is the singlet excitation energy and was determined approximately from the crossing point of the normalised absorption and emission spectra from **HBDPP** and **BBDPP** respectively in dichloromethane solution. A comparison of the HOMO and LUMO energies for **HBDPP**, **BBDPP** and the nitroaromatic quenchers as determined in SI.3 was also undertaken to estimate the favourability of electron transfer in each case.
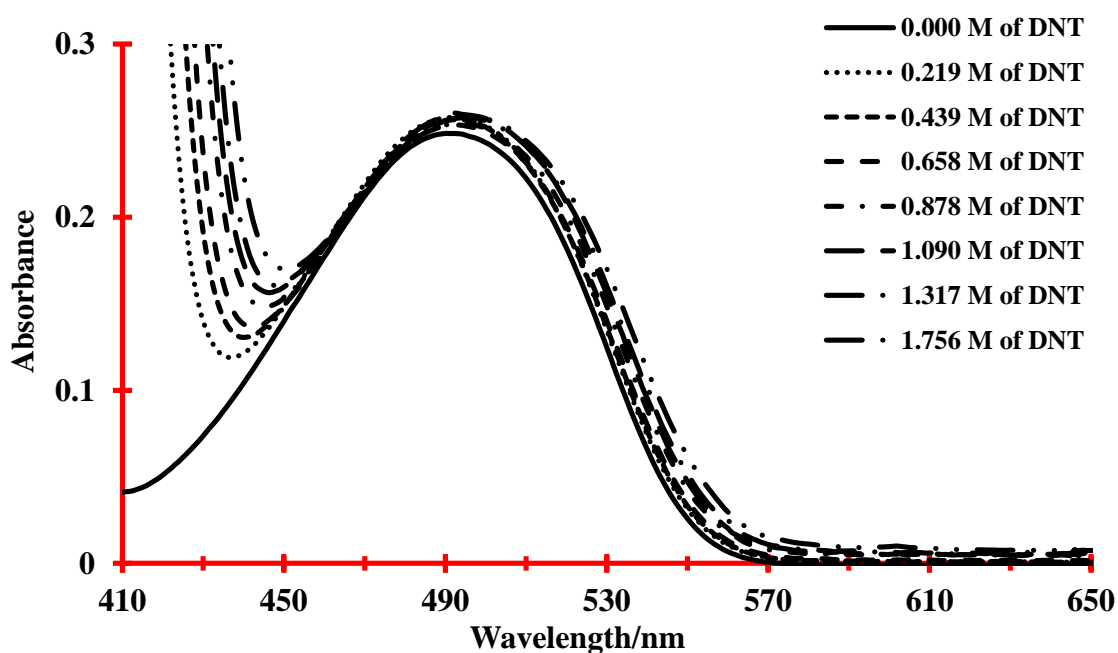

Figure S4.1. The effect on the UV/Vis absorption spectrum of **BBDPP** with increasing concentration of DNT. Lack of a substantive change in the absorption profile of **BBDPP** at high quencher concentration suggests that formation of a fluorophore/quencher ground state complex does not occur. A similar behaviour was observed for **HBDPP**, again indicative that ground state interactions between the DPP and nitroaromatic quenchers were not substantial.
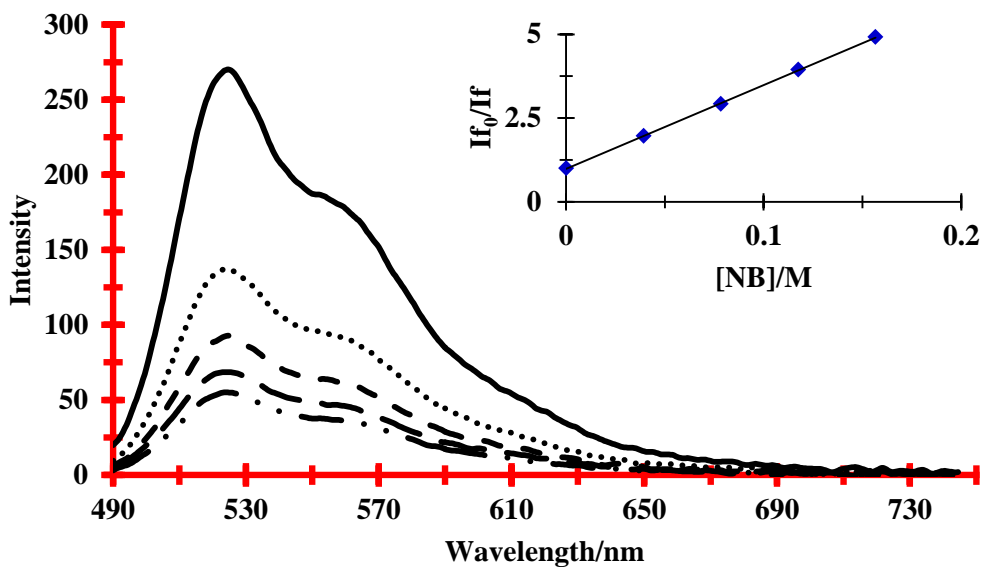
Figure S4.2. Fluorescence emission spectra of **HBDPP** quenched by increasing concentrations of **NB** in dichloromethane at 470 nm excitation wavelength. Inset depicts the generated linear Stern-Volmer plot measuring the intensity of fluorescence emission at 524 nm.

Figure S4.3. Fluorescence emission spectra of **HBDPP** quenched by increasing concentrations of **DNT** in dichloromethane at 470 nm excitation wavelength. Inset depicts the generated linear Stern-Volmer plot measuring the intensity of fluorescence emission at 524 nm.

Figure S4.4. Fluorescence emission spectra of **HBDPP** quenched by increasing concentrations of **TNT** in dichloromethane at 470 nm excitation wavelength. Inset depicts the generated linear Stern-Volmer plot measuring the intensity of fluorescence emission at 524 nm.
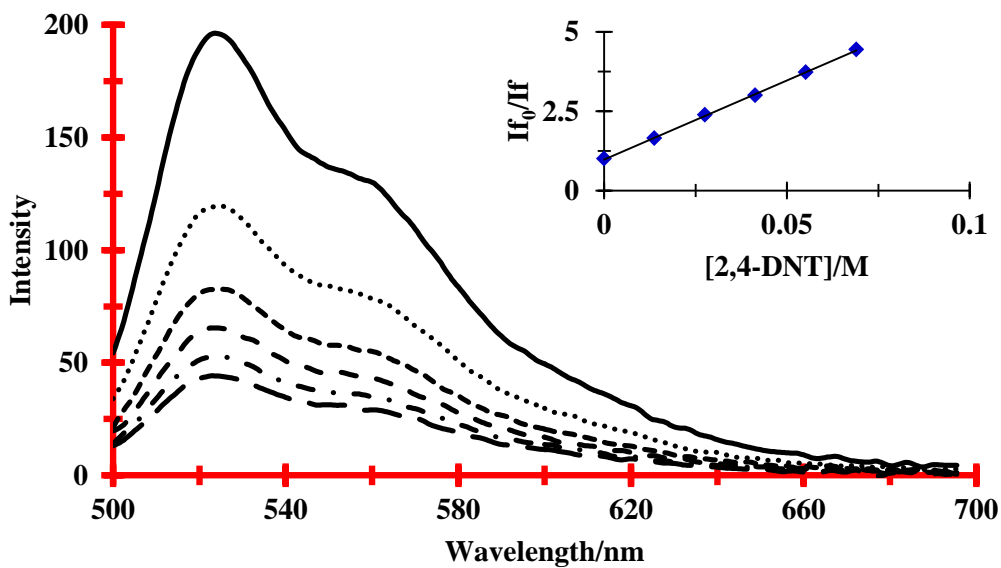

Figure S4.5. Fluorescence emission spectra of **BBDPP** quenched by increasing concentrations of **NB** in dichloromethane at 490 nm excitation wavelength. Inset depicts the generated linear Stern-Volmer plot measuring the intensity of fluorescence emission at 562 nm.
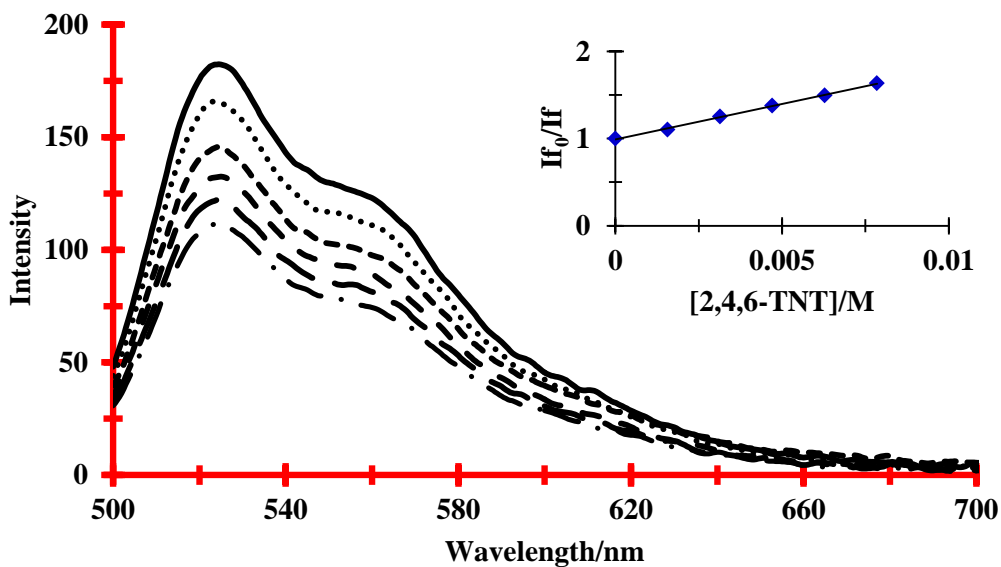
Figure S4.6. Fluorescence emission spectra of **BBDPP** quenched by increasing concentrations of **DNT** in dichloromethane at 470 nm excitation wavelength. Inset depicts the generated linear Stern-Volmer plot measuring the intensity of fluorescence emission at 562 nm.
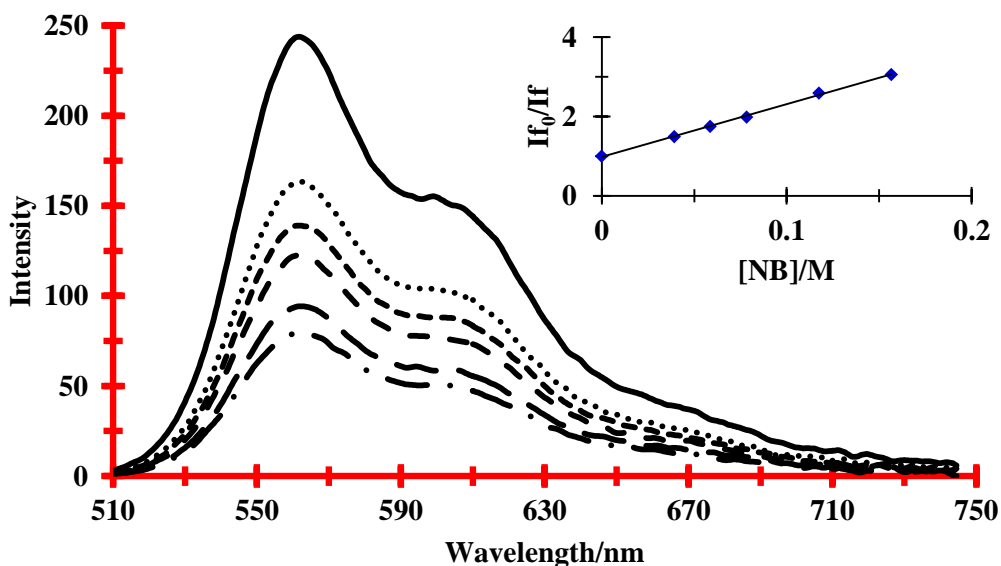

Figure S4.7. Fluorescence emission spectra of **BBDPP** quenched by increasing concentrations of **TNT** in dichloromethane at 480 nm excitation wavelength. Inset depicts the generated linear Stern-Volmer plot measuring the intensity of fluorescence emission at 562 nm.
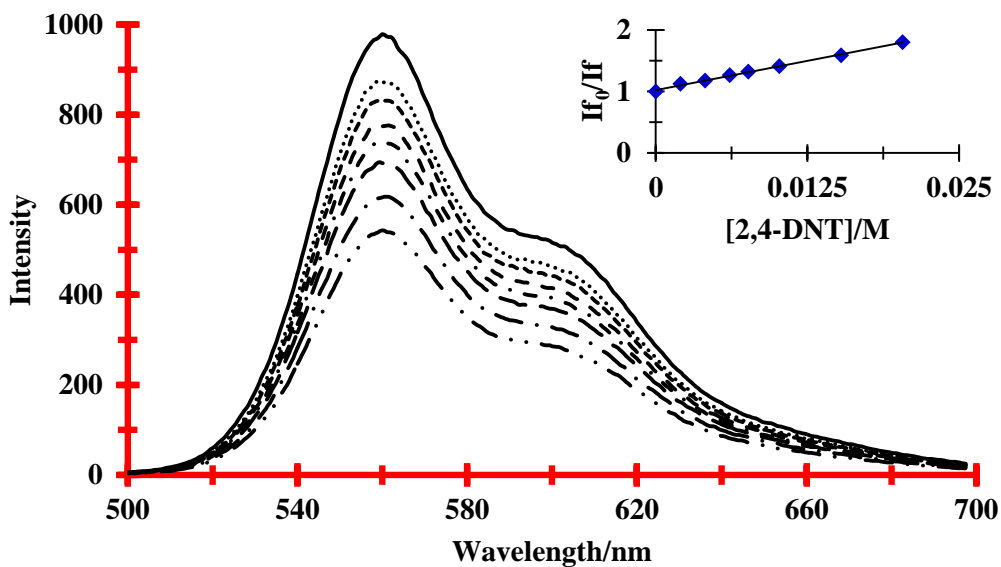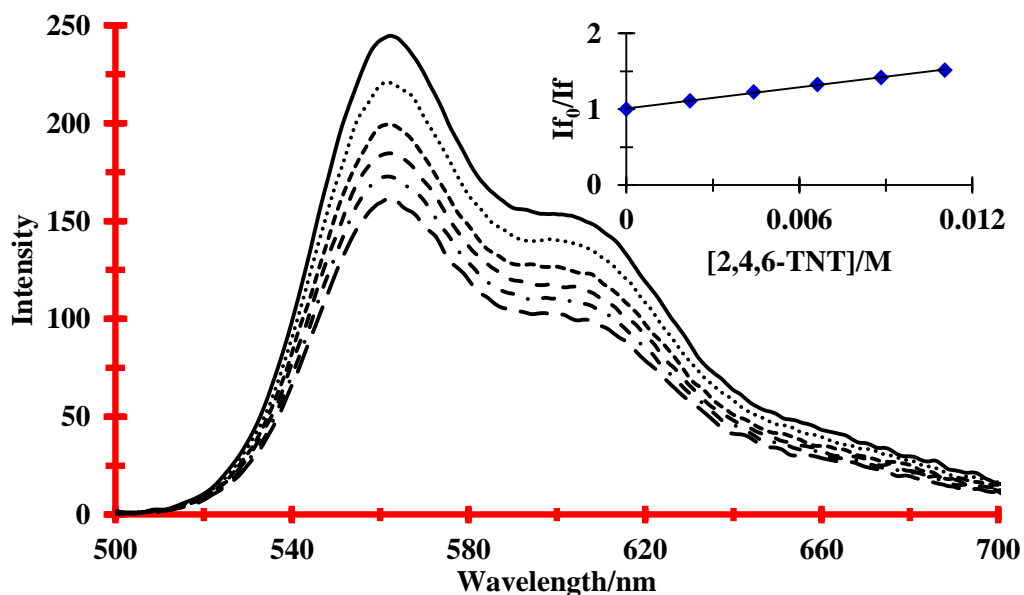
Table S4.1. Estimated diffusion controlled rate constants, k_d for quenching of **HBDPP** and **BBDPP** fluorescence with **NB**, **DNT** and **TNT** in dichloromethane. The Smoluchowski expression (Equation S4.1), which is known for overestimating the diffusion controlled rate constants,[13] gave an average value of 1.56 (±0.04) x 10^{10} $M^{-1}s^{-1}$; close to the values obtained experimentally from Stern-Volmer data and fluorescence lifetimes (see Table S4.2.).

Quencher	DPP	R_{DPP} (Å)	R_Q (Å)	k_d ($M^{-1}s^{-1}$)
NB	HBDPP	4.91	3.06	1.56×10^{10}
	BBDPP	5.83	3.06	1.63×10^{10}
DNT	HBDPP	4.91	3.36	1.53×10^{10}
	BBDPP	5.83	3.36	1.59×10^{10}
TNT	HBDPP	4.91	3.50	1.52×10^{10}
	BBDPP	5.83	3.50	1.57×10^{10}

Table S4.2. Experimentally determined Stern-Volmer constants (K_{sv}) for the fluorescence quenching of **HBDPP** and **BBDPP** with **NB**, **DNT** and **TNT** in dichloromethane and derived quenching rate constants (kq). Fluorescence lifetimes in the absence of quencher, τ_0 were 6.46 ns for **HBDPP** and 3.95 ns for **BBDPP**. Also included are the experimentally determined DPP and nitroaromatic oxidation and reduction potentials (vs. SCE), $E_{0,0}$ energies for **HBDPP** and **BBDPP** (obtained from the crossing point of their absorption and emission spectra) and the Gibbs free energy changes for electron transfer (ΔG), derived using Equation S4.2. In all cases ΔG was negative, indicating a thermodynamically favourable driving force for electron transfer.

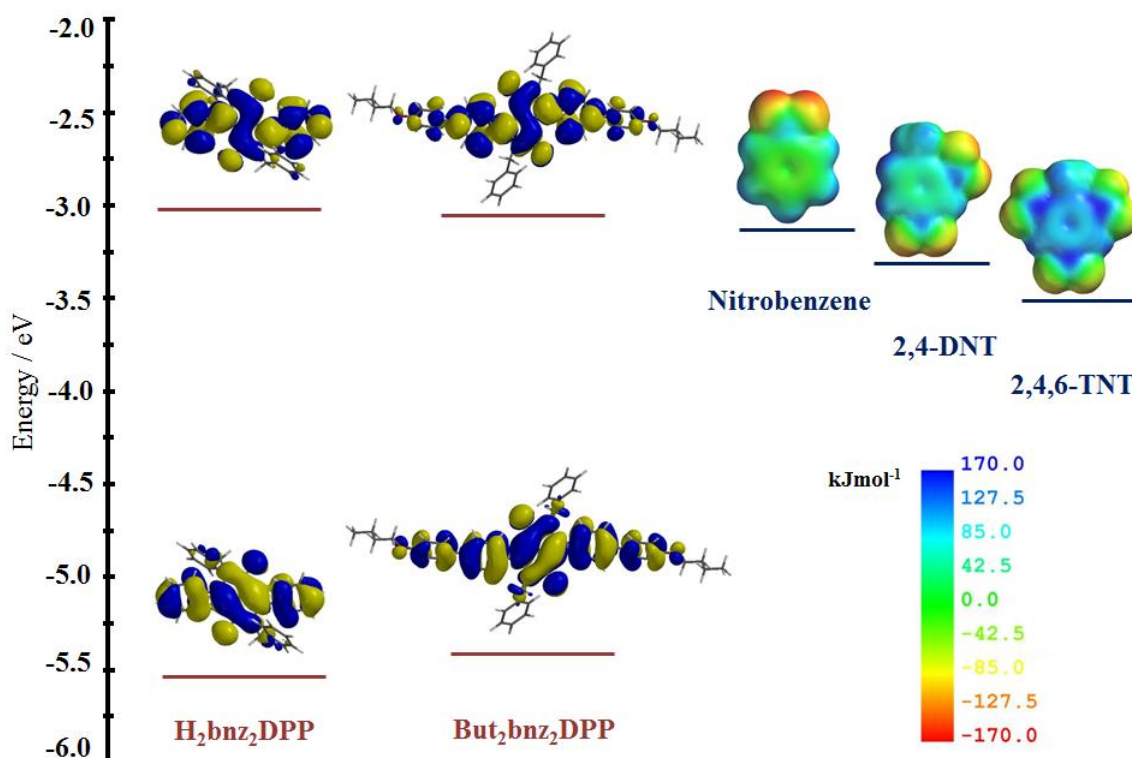| DPP (D)	Quencher (A)	K_{sv} (M^{-1})	k_q ($M^{-1}s^{-1}$)	E (D^+/D) (eV)	E (A/A) (eV)	$E_{0,0}$ (eV)	ΔG (eV)
HBDPP	NB	25.0	3.84×10^9	+1.244	-1.116	2.463	-0.103
	DNT	49.9	7.67×10^9	+1.244	-0.901	2.463	-0.317
	TNT	81.3	12.50×10^9	+1.244	-0.657	2.463	-0.562
BBDPP	NB	13.3	3.33×10^9	+1.125	-1.116	2.311	-0.070
	DNT	38.0	9.50×10^9	+1.125	-0.901	2.311	-0.285
	TNT	46.2	11.60×10^9	+1.125	-0.657	2.311	-0.530

Figure S4.8. HOMO and LUMO energies (with respective Kohn-Sham orbitals) for **HBDPP** and **BBDPP** (left). HOMO and LUMO energies (and electrostatic potential surfaces) for **NB**, **DNT** and **TNT** (right). Orbital energies were determined from the experimentally obtained oxidation and reduction potentials using Ferrocene as standard (described in SI3), as this approach has been extensively employed previously to demonstrate favourable electron transfer energetics in nitroaromatic sensing.[14-16] Kohn-Sham orbitals for **HBDPP** and **BBDPP** and electrostatic surfaces for **NB**, **DNT** and **TNT** were calculated from optimised geometries of each system, employing M06-2X/6-31G(d) in all cases. Relative ordering of the respective orbital energies is consistent in this case, (despite the accepted limitations of the methodology employed)[17] with a thermodynamically favourable driving force for electron transfer between **HBDPP** and **BBDPP** and each of the nitroaromatics.

SI.5. Thin Film Fabrication and Characterisation and Solid State Fluorescence Quenching

Thin Film Fabrication and Characterisation: Thin films of **HBDPP** and **BBDPP** were prepared by spin coating onto silica discs (20 mm diameter) from dichloromethane solution using an SPC Spin 150 Coater (Table S5.1). Amorphous thin films were prepared by spin coating solutions that had been filtered through a 0.45 μm frit, whilst the more highly ordered, *as-deposited* films, were obtained by spin coating solutions containing microcrystalline seeds of the DPP. After spin coating the thin films were dried at room temperature prior to analysis or quenching experiments. Films of varying thickness were prepared by changing the concentration of DPP solution used during spin coating. The film thickness was measured using a Veeco Dektak³ST surface profiler, and SEM images of the films were determined using a Hitachi S4100 cathode field emission SEM, employing an Oxford Instruments Germanium EDX detector with resolution of 115eV. Optical characterisation of thin films by UV-Vis absorption spectroscopy and fluorescence spectroscopy was as described in SI.3.

Table S5.1. Spin coating parameters employed in the fabrication of **HBDPP** and **BBDPP** amorphous and ordered *as-deposited* thin films.

Program	Step 1	Step 2
Time	10 seconds	30 seconds
RPM	800	2000
RPM/s²	3000	3000

Table S5.2. Concentration of DPP solutions in dichloromethane employed in the fabrication of **HBDPP** and **BBDPP** amorphous and ordered *as-deposited* thin films and respective film thickness.

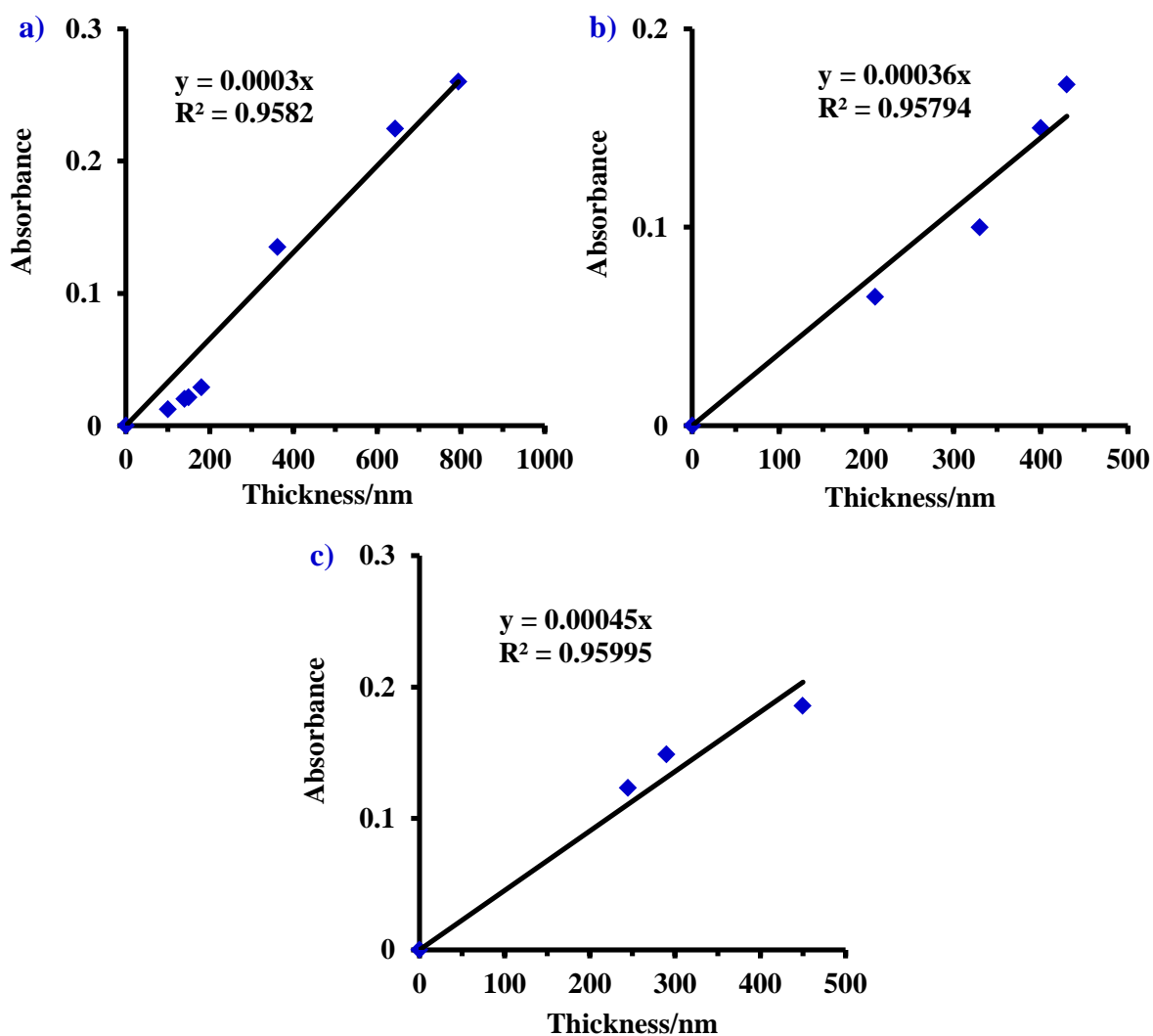|	Concentration (mg/ml)	Approximate Film Thickness (nm)
HBDPP	0.5	150
	1.0	300
	2.5	600
	5.0	900
BBDPP	0.5	100
	1.0	200
	2.5	400
	5.0	500

Figure S5.1. Correlation between thin film thickness determined via surface profiling and film absorbance for a) amorphous **HBDPP** films, b) amorphous **BBDPP** films and c) ordered, *as-deposited* **BBDPP** films.

Solid State Fluorescence Quenching: Quenching of thin film emission was conducted using a modified version of the method reported by Swager, [18,19] where the UV-Vis absorption and emission spectra of the film were recorded before and then during exposure to **DNT** or **NB**.

To carry out the time dependence analysis, films of **HBDPP** or **BBDPP** were placed in a pre-fabricated sample holder designed to fit into the UV-Vis and fluorescence instruments described in SI.3. This ensured that the same part of the film was interrogated during quenching to avoid issues relating to film inhomogeneity such as variable photon absorption. For exposure to explosive vapours the sample holder with film, was placed into a separate pre-fabricated chamber containing a small quantity of nitroaromatic covered by cotton wool which had been pre-equilibrated overnight at 25 °C to ensure a saturated headspace of nitroaromatic vapour. The film sample holder was attached to the chamber, presenting the

film surface to nitroaromatic vapour and avoiding any direct contact of the film with the condensed explosive material. During quenching experiments, the sample holder with film was removed for spectroscopic interrogation and replaced carefully into the sample chamber in order to minimise any possible loss of nitroaromatic headspace vapour.
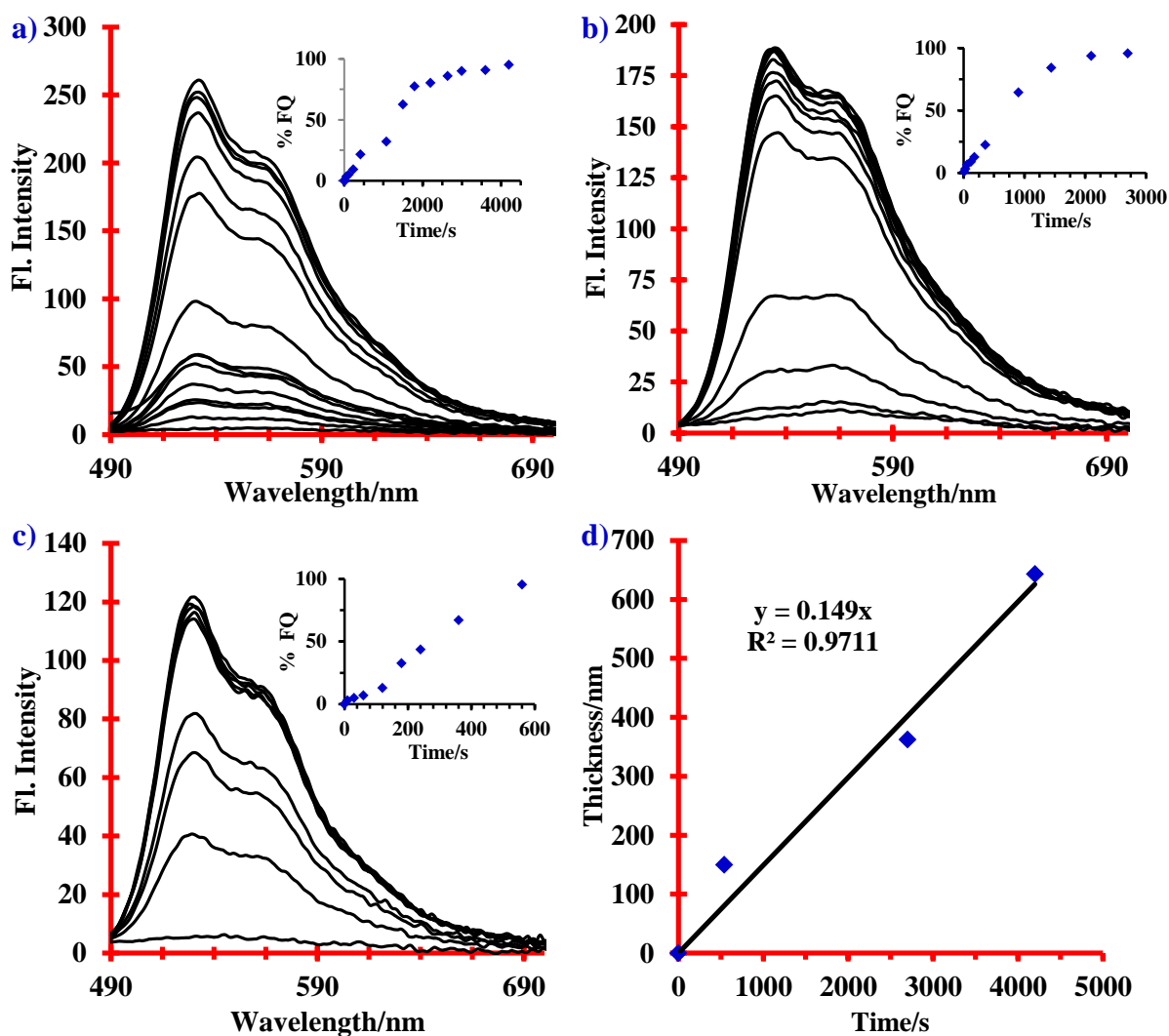

Figure S5.2. Emission spectra and inset showing fluorescence quenching as a function of time at 530 nm for **HBDPP** amorphous thin films of a) 643 nm thickness, b) 362 nm thickness and c) 150 nm thickness upon exposure to **NB** vapour (Excitation in all cases at 430 nm). The correlation between film thickness of amorphous films of **HBDPP** and the time to reach complete emission quenching for each of the films is shown in d).
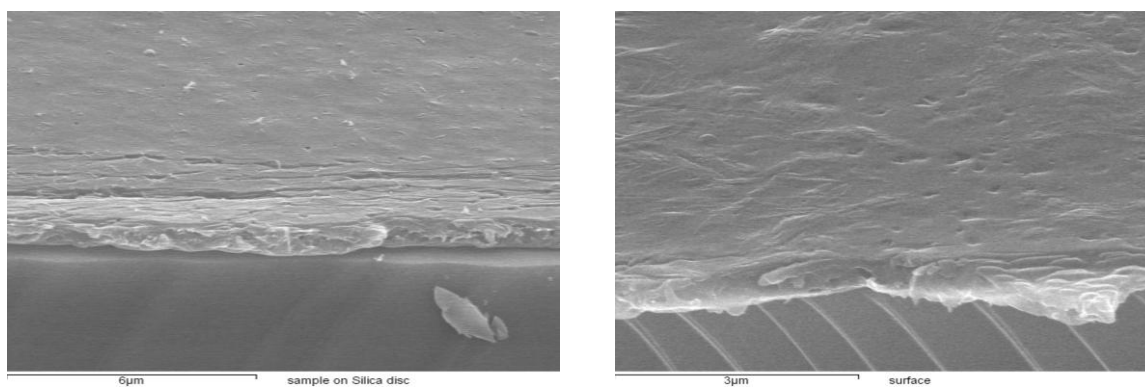
Figure S5.3. SEM images taken of amorphous **HBDPP** thin film before (left) and after (right) exposure to **NB** vapour. The images confirm that there were no significant changes to the film morphology after **NB** exposure resulting from crystallisation (vide infra).
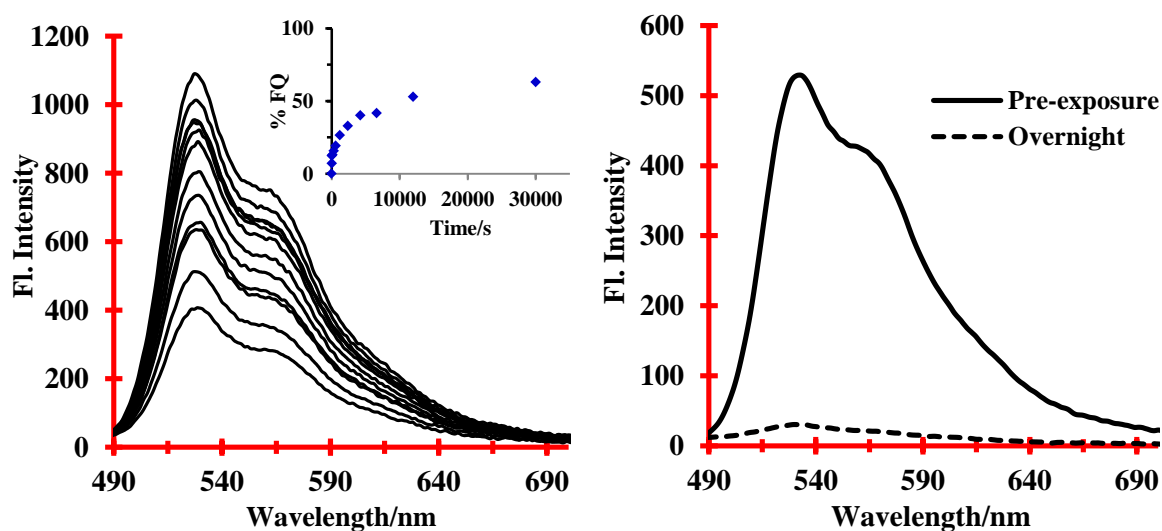

Figure S5.4. Emission spectra and inset showing fluorescence quenching as a function of time at 530 nm (Excitation at 430 nm) for a 180 nm **HBDPP** amorphous thin film upon exposure to **DNT** vapour (left). Emission spectra for a 360 nm **HBDPP** amorphous thin film (Excitation at 450 nm) upon prolonged exposure to **DNT** vapour showing complete quenching of fluorescence (right).
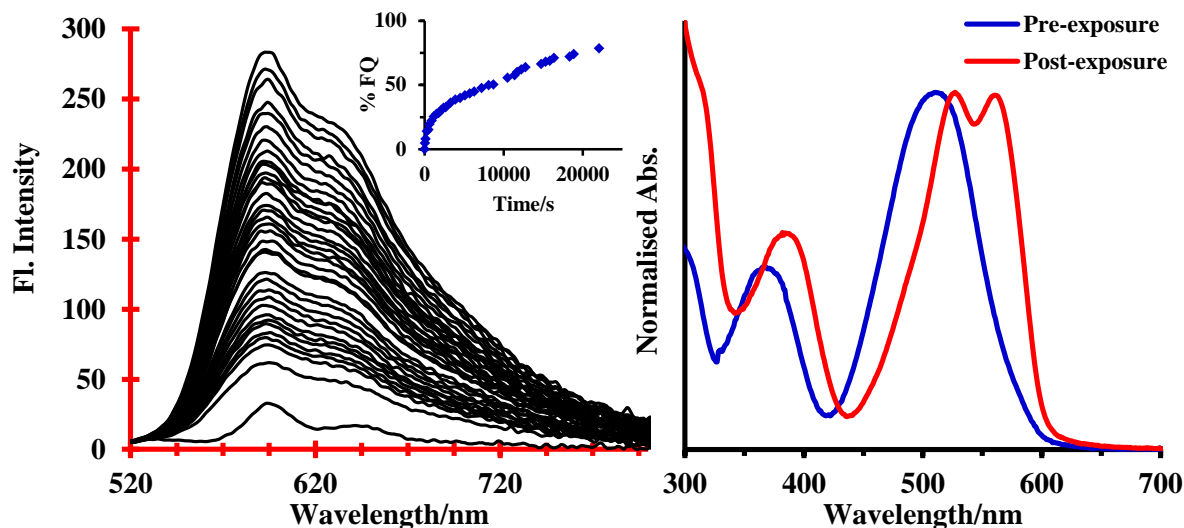
Figure S5.5. Emission spectra and inset showing fluorescence quenching as a function of time at 593 nm (Excitation at 490 nm) for a 210 nm **BBDPP** amorphous thin film upon exposure to **DNT** vapour (left). Normalised UV-Vis absorption spectra of the same **BBDPP** film before and after exposure to **DNT** vapour (right). The change in film UV-Vis absorption spectrum is consistent with conversion to a more ordered structure, similar to that obtained by spin coating seeded solutions of **BBDPP**.
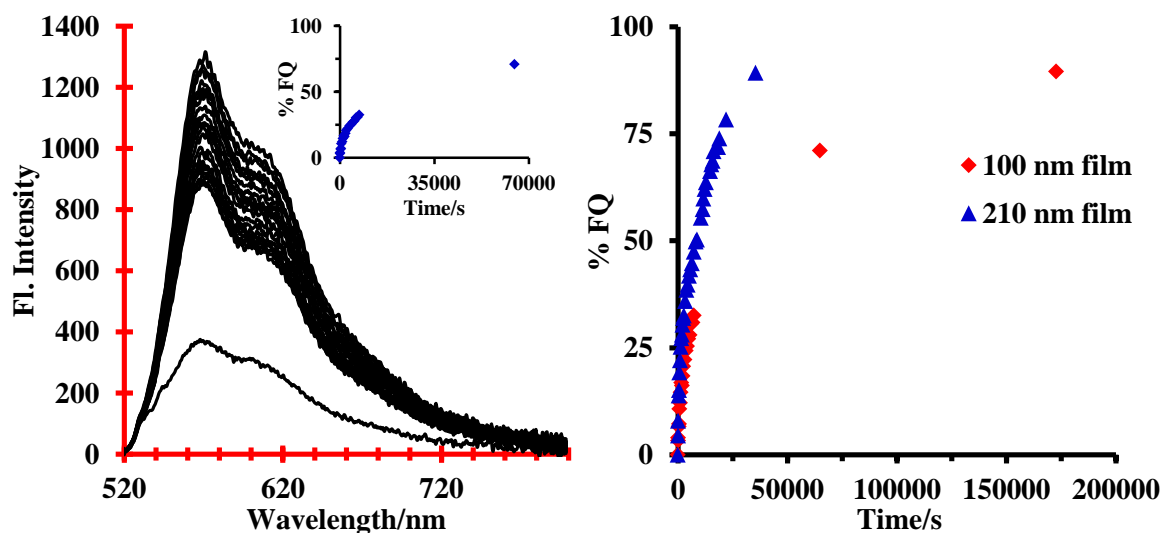

Figure S5.6. Emission spectra and inset showing fluorescence quenching as a function of time at 570 nm (Excitation at 500 nm) for a 100 nm **BBDPP** amorphous thin film upon exposure to **DNT** vapour (left). Comparison of film thickness on the rate of fluorescence quenching for 100 nm and 210 nm amorphous films of **BBDPP** showing a more rapid reduction in emission intensity for the thicker film, with both films achieving the same saturation decay in fluorescence upon exposure to **DNT** vapour (right).
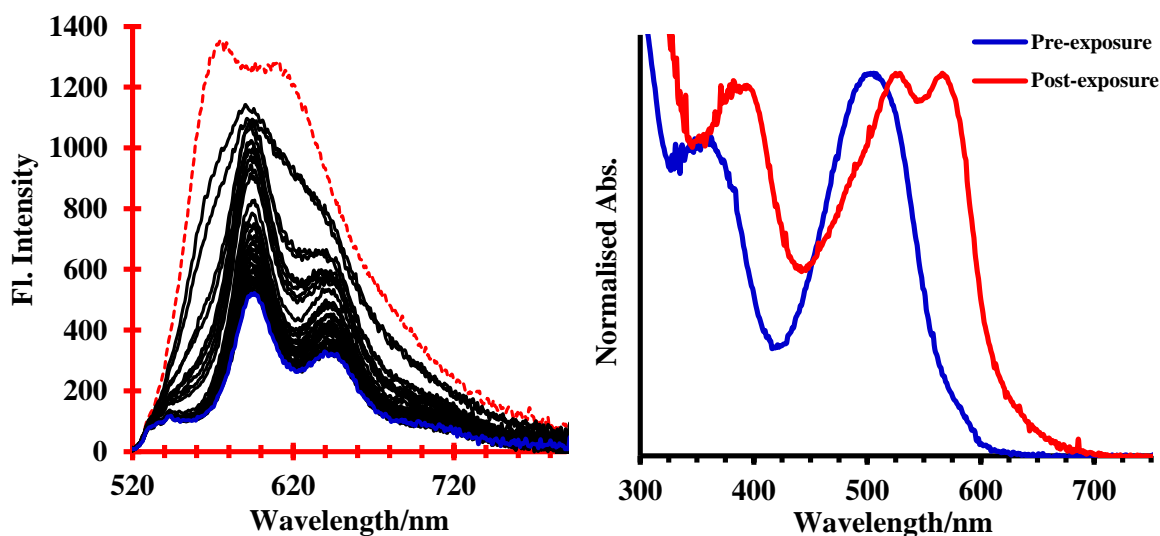
Figure S5.7. Emission spectra showing a reduction in emission intensity (Excitation at 490 nm) for 100 nm **BBDPP** amorphous thin film upon exposure to **NB** vapour (left). The emission spectral line shape changes during exposure to **NB** (initial dotted red line changing to blue solid line) indicating a significant change in the film structure. Normalised UV-Vis absorption spectra of the same **BBDPP** film before and after exposure to **NB** vapour (right). The change in film UV-Vis absorption spectra is again consistent with conversion to a more ordered structure, similar to that obtained by spin coating seeded solutions of **BBDPP**.
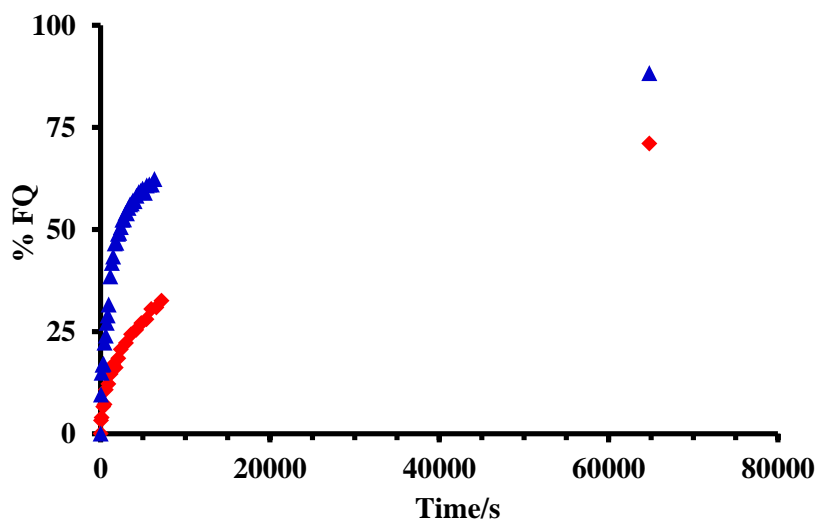

Figure S5.8. Fluorescence quenching as a function of time for 100 nm **BBDPP** amorphous thin films upon exposure to **DNT** vapour (♦) and **NB** vapour (▲), indicating a faster overall response of these films to **NB**.
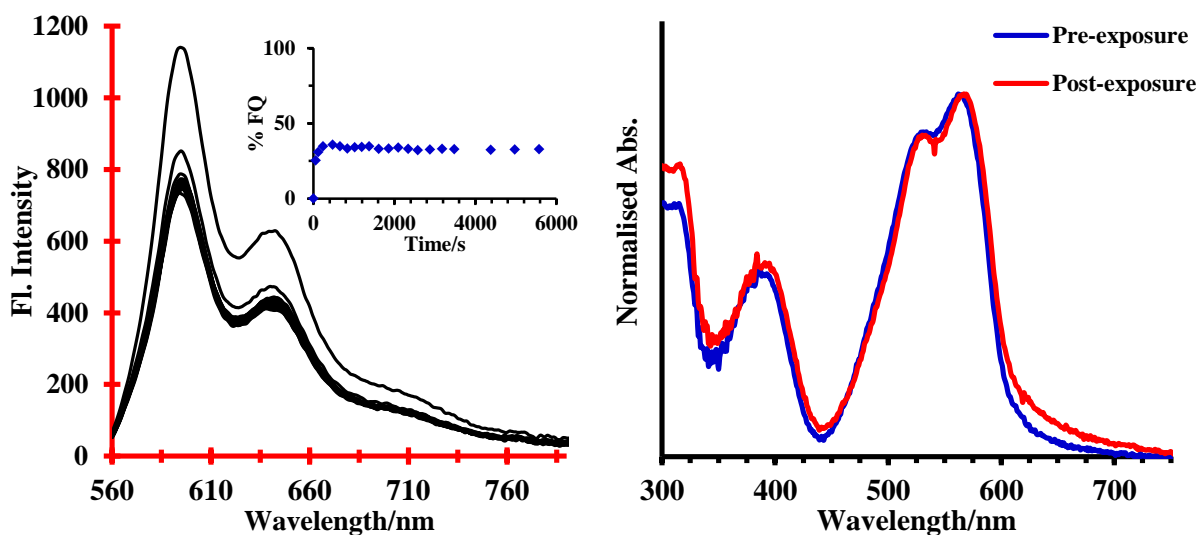
Figure S5.9. Emission spectra and inset showing fluorescence quenching as a function of time at 597 nm (Excitation at 540 nm) for a 100 nm **BBDPP** ordered *as-deposited* thin film upon exposure to **NB** vapour (left). Normalised UV-Vis absorption spectra of the same **BBDPP** film before and after exposure to **NB** vapour (right) showing no significant changes in spectral profile.

Figure S5.10. Emission spectra and inset showing fluorescence quenching as a function of time at 597 nm (Excitation at 540 nm) for a 100 nm **BBDPP** ordered *as-deposited* thin film upon exposure to **DNT** vapour (left). Normalised UV-Vis absorption spectra of the same **BBDPP** film before and after exposure to **DNT** vapour (right) showing no significant changes in spectral profile.
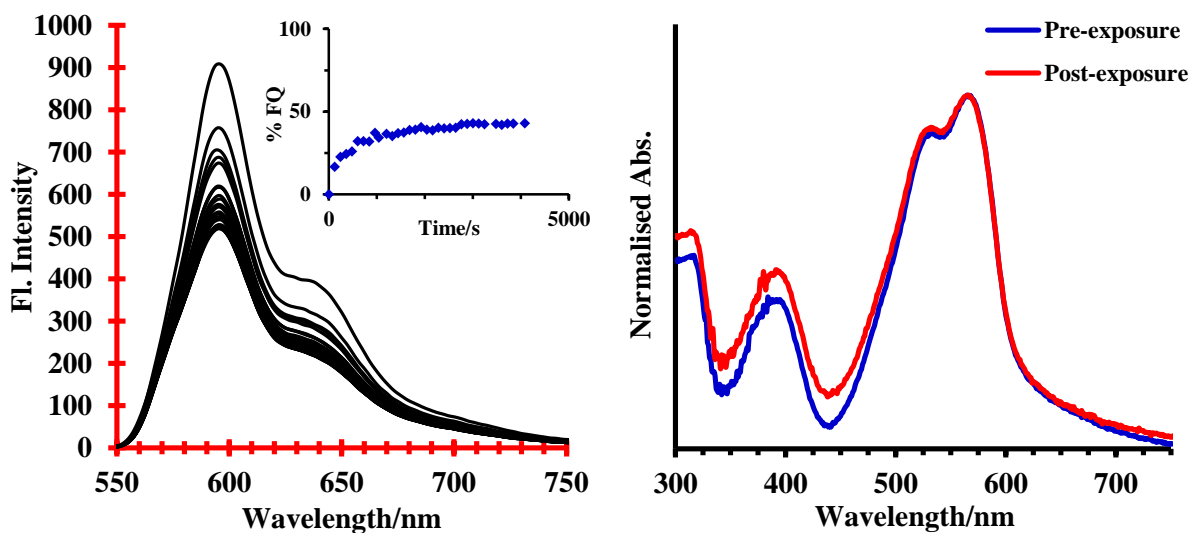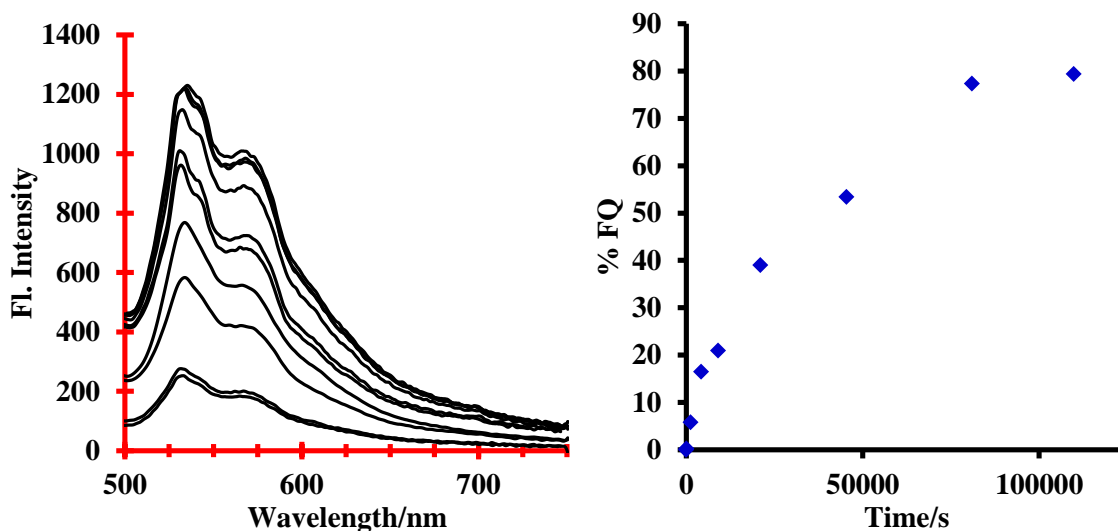
Figure S5.11. Emission spectra showing a reduction in emission intensity at 535 nm (Excitation at 450 nm) for a 150 nm **HBDPP** ordered *as-deposited* thin film upon exposure to **DNT** vapour (left) and reduction in emission intensity at 535 nm as a function of time (right).
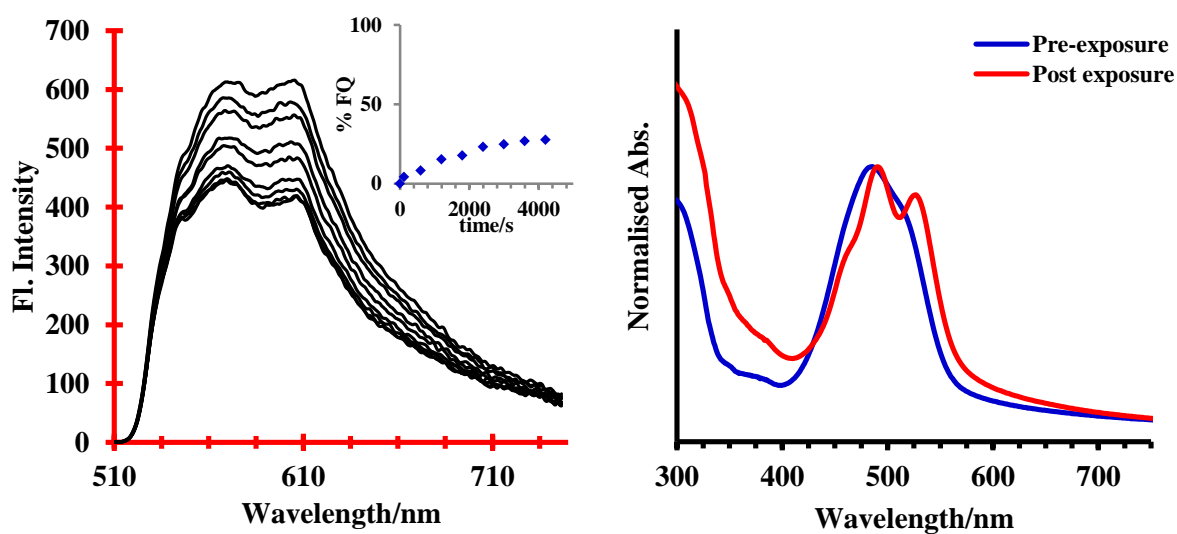
Figure S5.12. Emission spectra and inset showing fluorescence quenching as a function of time at 570 nm (Excitation at 450 nm with a filter at 520 nm to reduce effects of scatter) for a 350 nm **HBDPP** ordered *as-deposited* thin film upon exposure to **NB** vapour (left). Normalised UV-Vis absorption spectra of the same **HBDPP** film before and after exposure to **NB** vapour (right) indicating a considerable change in spectral profile associated with enhanced film crystallinity and a change in film morphology (vide infra) (right).

Figure S5.13. SEM images taken of ordered *as-deposited* **HBDPP** thin film before (left) and after (right) exposure to **NB** vapour. The images confirm significant changes to the film morphology after **NB** exposure resulting from solvent induced crystallisation/annealing which is consistent with the characteristic changes in the UV-Vis absorption spectrum.

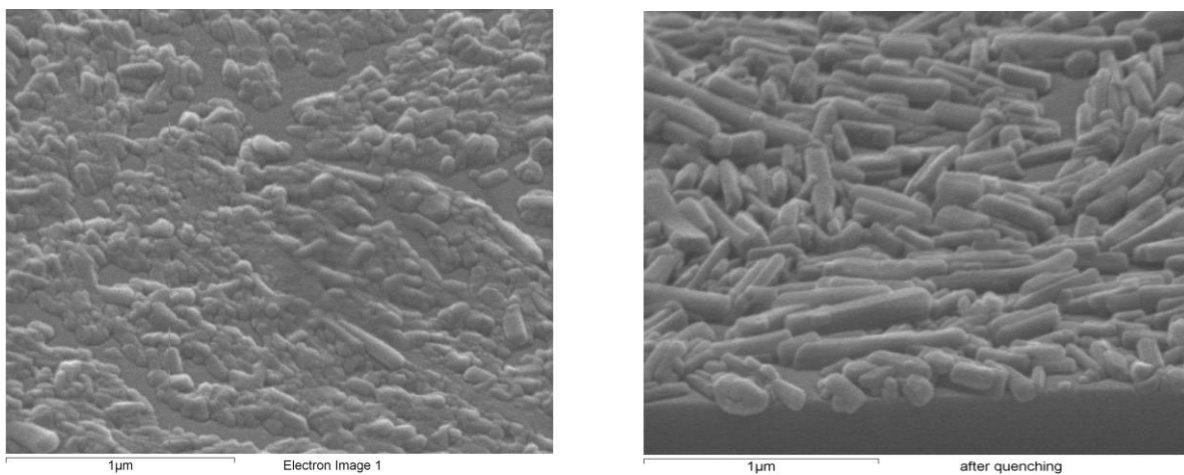## SI.6. Effect of Solvent Annealing on the Structure and Optical Properties of HBDPP and BBDPP Thin Films

Transmission X-ray diffraction data collection from a powder sample of HBDPP:

A sample of **HBDPP** was lightly dispersed in an agate mortar and pestle, before being filled into a 0.7 mm borosilicate glass capillary and mounted and aligned on a Bruker-AXS D8 diffractometer. PXRD data were collected at *RT* over the range 3.5–55° 2θ (2 kW; Cu $K_{\alpha 1}$, 1.54056 Å; step size 0.017°; 10 s per step; LynxEye detector).
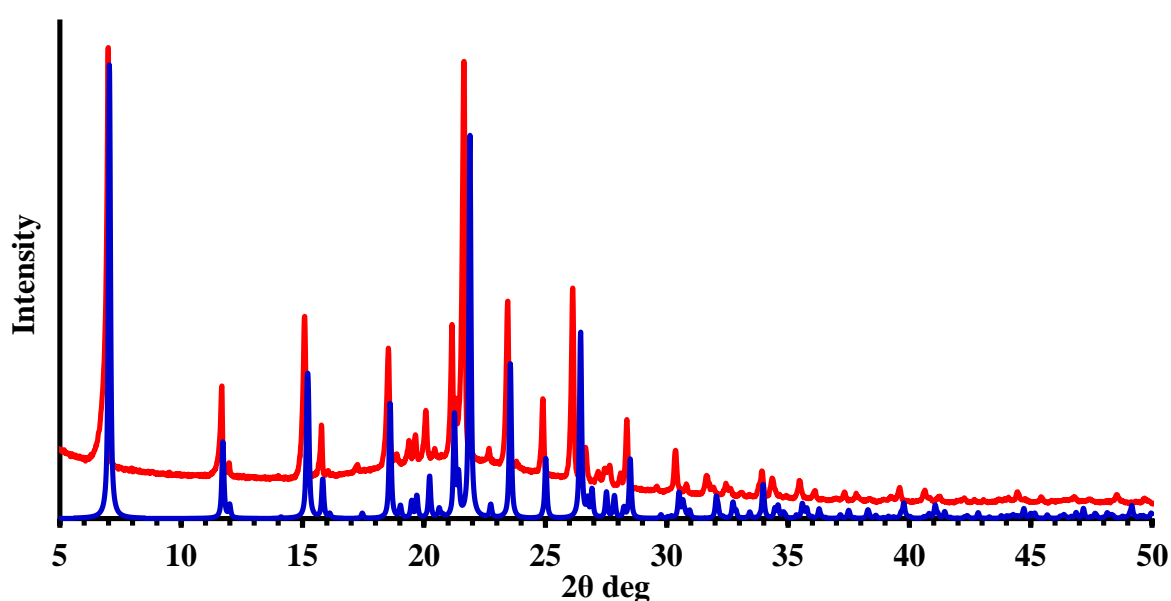
Figure S6.1. PXRD pattern from **HBDPP** bulk powder (top, red) and predicted XRD pattern determined in Mercury from single crystal X-ray structure (bottom, blue).

The *RT* monochromatic capillary transmission powder X-ray diffraction (PXRD) data for **HBDPP** were Pawley-fitted satisfactorily in the program TOPAS (5 − 55° 2θ), starting from the triclinic lattice parameters and space group (*P*-1) reported for the *RT* single-crystal (SX) structure of **HBDPP**. Across the pattern, the fit to the data is good, yielding refined *RT* unit cell parameters that are in excellent agreement with the SX structure (see table below and **Figure S6.2**).

HBDPP data	*a* / Å	*b* / Å	*c* / Å	α / °	β / °	γ / °	*V* / Å³
RT PXRD	5.89257(17)	7.8546(2)	13.1537(6)	74.973(2)	83.985(3)	86.9726(19)	584.54(4)
RT SX	5.8880(6)	7.8567(12)	13.1487(18)	74.959(13)	83.973(10)	86.915(10)	583.95(13)
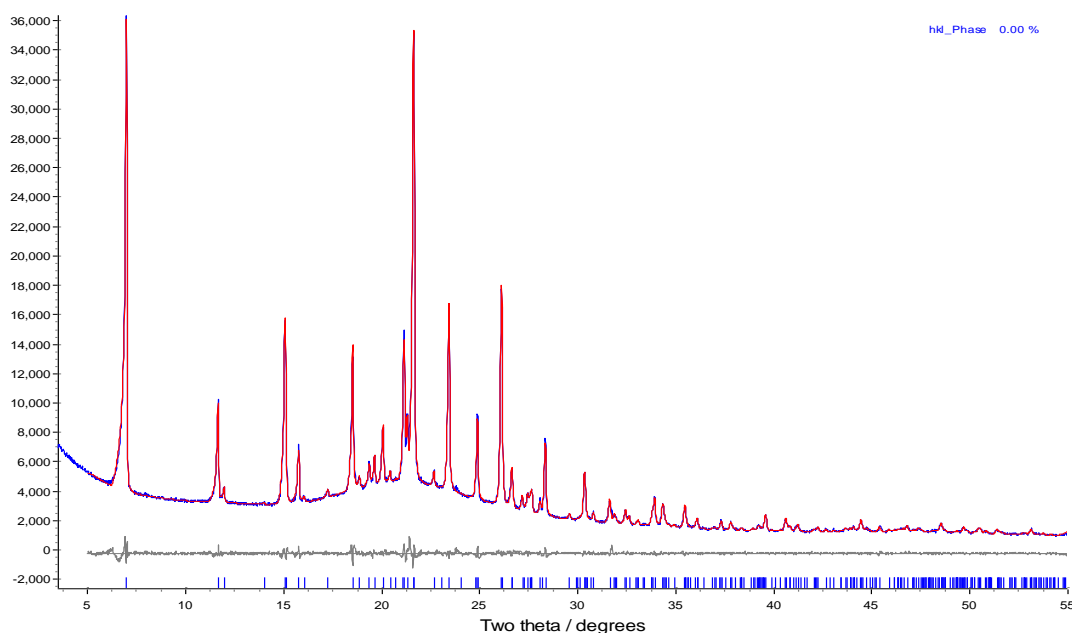
Figure S6.2. The result of a Pawley refinement using **HBDPP** unit cell parameters and *RT* PXRD data in the range 5 - 55° 2θ [R_{wp} = 2.80, zero point error = 0.0042(4); **blue** = observed pattern, **red** = calculated profile (generated from the refinement), **grey** = difference between observed and calculated]. Tick marks along the bottom of the plot highlight the calculated reflection positions.

Reflection XRD data collection from solvent-annealed films of HBDPP:

Solvent treatment of *as-deposited* ordered thin films was carried out using the approach employed during solid state fluorescence quenching (SI.5), with nitroaromatic samples replaced by neat acetone or toluene. An acetone annealed film of **HBDPP** was deposited onto a quartz zero background diffraction plate. The plate was then attached to a sample holder (see image below) using 'Blu Tack' adhesive (note that the adhesive does not contribute to the diffraction pattern). The sample holder was mounted on a Bruker-AXS D8 diffractometer and diffraction data were collected at *RT* over the range 3.5–65° 2θ (2 kW; Cu $K_{\alpha 1}$, 1.54056 Å; step size 0.017°; 5 s per step; LynxEye detector). XRD patterns of **HBDPP** thin films on scattering SiO_2 substrates were similarly collected at *RT* over the range of 5-40° 2θ using a Siemens D5000 diffractometer (Cu Kα, 40 kV/30 mA).
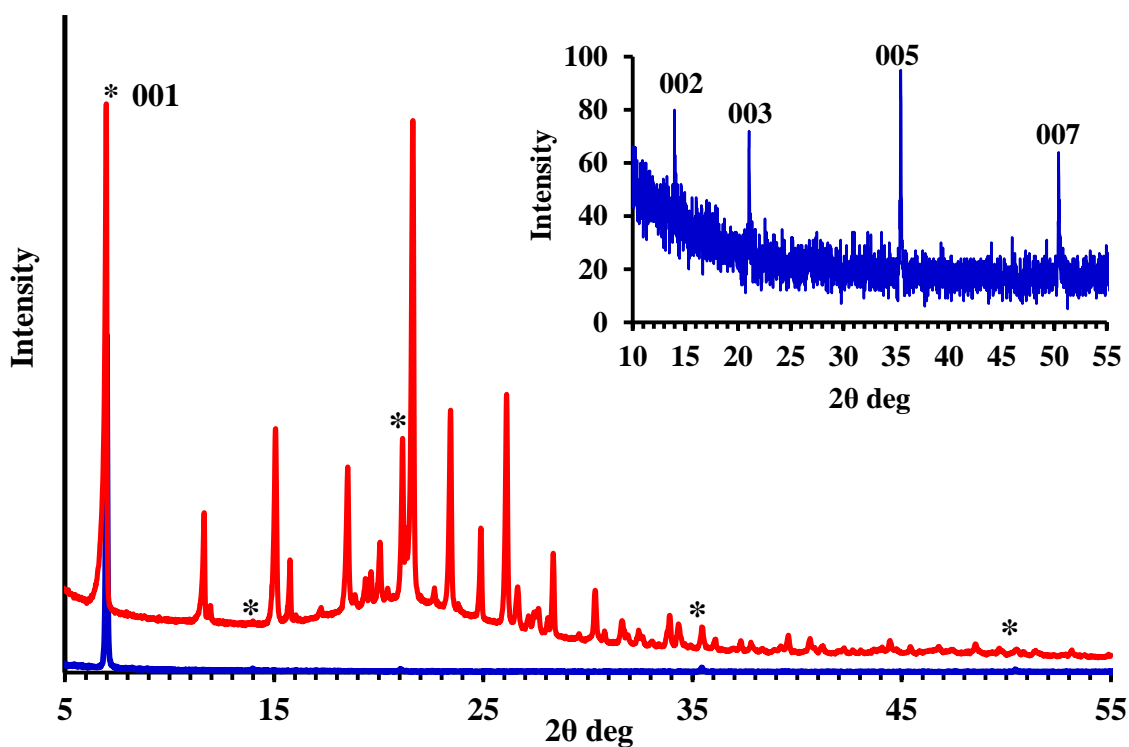
Figure S6.3. PXRD pattern for **HBDPP** powder (top, red) and XRD pattern for **HBDPP** acetone annealed thin film (bottom, blue) on non-scattering SiO₂. Those reflections observed in the thin film XRD pattern are highlighted and magnified (inset) with their respective *00l* planes shown, as determined from the calculated single crystal XRD pattern in Mercury.
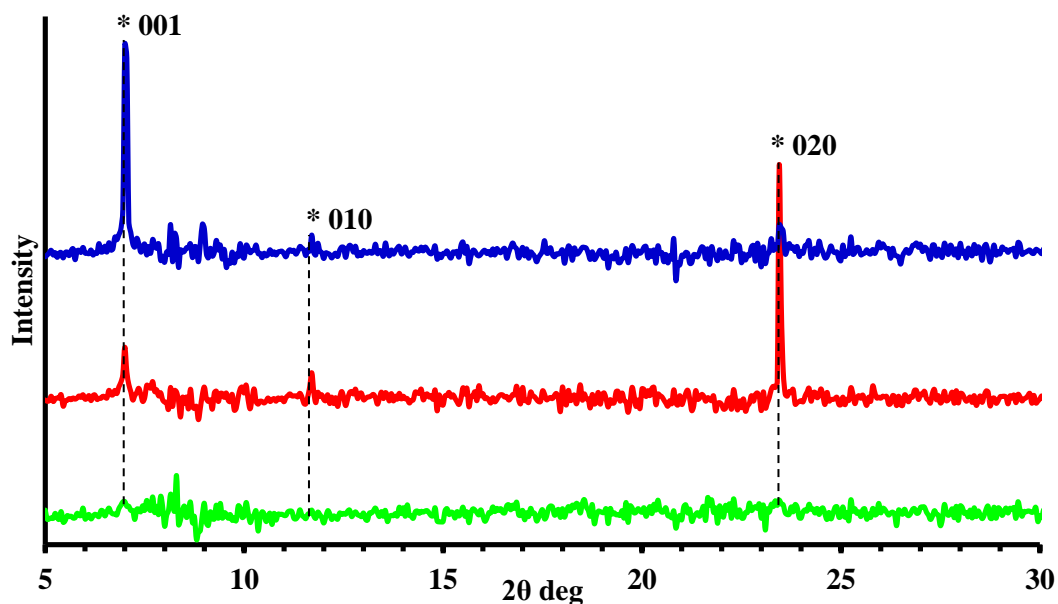
Figure S6.4. XRD patterns for acetone (top, blue), and toluene (middle, red) annealed thin films of **HBDPP** on SiO₂. A pre-annealed thin film XRD pattern is shown (bottom, green). XRD patterns have been corrected for the background substrate (SiO₂) scatter and intensity offset for clarity. Reflections are highlighted with respective *hkl* planes as determined from the single crystal X-ray structure in Mercury.

Figure S6.5. Schematic representation showing proposed orientations of **HBDPP** crystals on SiO$_2$ substrates after acetone or toluene annealing as determined by XRD analysis. In both cases, the cofacial stacking a-axis (100 plane) is orientated parallel to the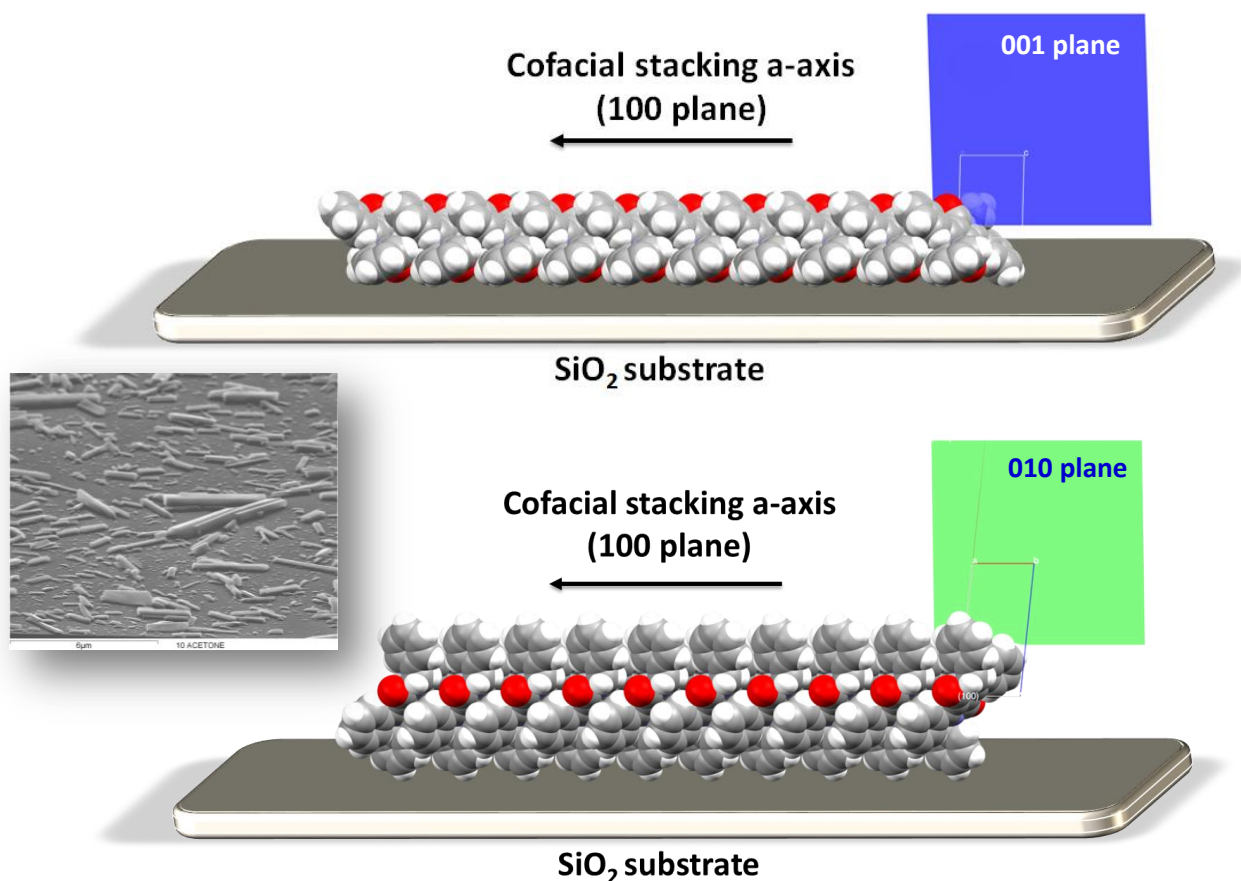 substrate, as evidenced from the XRD data shown in Figures S6.3 and S6.4, where reflections from this plane were not detected employing the Bragg-Brentano reflection geometry. Thus, the needle like crystals observed by SEM analysis (acetone annealed thin film shown above) are orientated with the π-stacking a-axis parallel to the SiO$_2$ substrate and directed along the long dimension in the crystal aspect.

Table S6.1. Crystal surface area determination for an acetone annealed **HBDPP** thin film from SEM analysis of crystallites (see **Figure S6.6** below for details of the individual crystals from which the data was selected). From the total surface area the % of end face surface to the total surface area was calculated and found to be on average approximately 7-8 % of the total crystal surface area, consistent with the saturation quenching levels observed from these thin films.

Crystal	Length (nm)	Width (nm)	Height (nm)	Surface Area (nm^2)	End Faces Surface Area (nm^2)	% End Face Surface Area/Total
1	1472	288	176	1467392	101376	6.9%
2	1440	272	192	1440768	104448	7.2%
3	1152	208	192	1001472	79872	8.0%
4	1152	176	176	872960	61952	7.1%
5	432	96	192	285696	36864	12.9%
6	1888	160	224	1521664	71680	4.7%
7	1552	112	160	880128	35840	4.1%
8	816	112	144	450048	32256	7.2%

|						
9	464	240	112	380416	53760	14.1%
10	720	176	112	454144	39424	8.7%
11	928	96	176	538624	33792	6.3%
12	1216	32	96	317440	6144	1.9%
13	1024	112	144	556544	32256	5.8%
14	384	160	96	227328	30720	13.5%
15	544	96	128	268288	24576	9.2%
16	672	64	64	180224	8192	4.5%
17	608	48	96	184320	9216	5.0%
18	2080	144	128	1168384	36864	3.2%
19	704	64	96	237568	12288	5.2%
20	1024	96	96	411648	18432	4.5%
21	816	64	96	273408	12288	4.5%
22	512	64	144	231424	18432	8.0%
23	960	96	64	319488	12288	3.8%
24	800	32	32	104448	2048	2.0%
25	320	112	96	154624	21504	13.9%
26	624	32	80	144896	5120	3.5%
27	656	112	128	343552	28672	8.3%
28	672	112	96	301056	21504	7.1%
29	672	64	176	345088	22528	6.5%
30	544	64	128	225280	16384	7.3%
31	320	144	80	166400	23040	13.8%
32	800	80	64	240640	10240	4.3%
33	352	64	80	111616	10240	9.2%
34	592	48	64	138752	6144	4.4%
35	640	64	96	217088	12288	5.7%
36	864	32	32	112640	2048	1.8%
37	512	112	96	234496	21504	9.2%
38	624	80	64	189952	10240	5.4%
39	320	160	192	286720	61440	21.4%
40	960	288	144	912384	82944	9.1%
41	512	128	96	253952	24576	9.7%
42	1280	64	240	808960	30720	3.8%
43	544	80	80	186880	12800	6.8%
44	672	80	96	251904	15360	6.1%
45	304	80	64	97792	10240	10.5%
					Average	7.2%
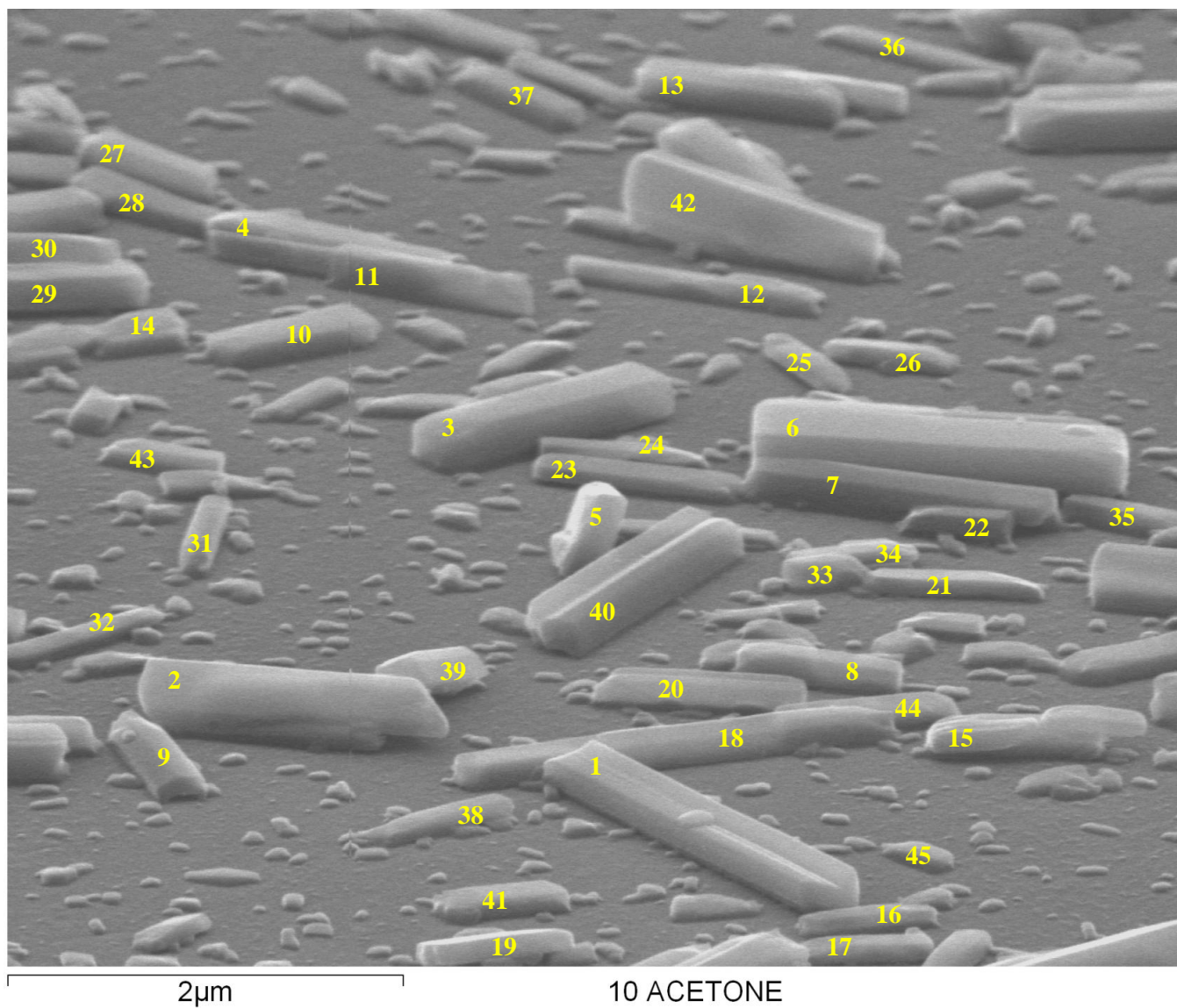
Figure S6.6. SEM of an acetone annealed **HBDPP** thin film. Numbered crystals are those used in the surface area determinations and their respective dimensions are collated in **Table S6.1**.
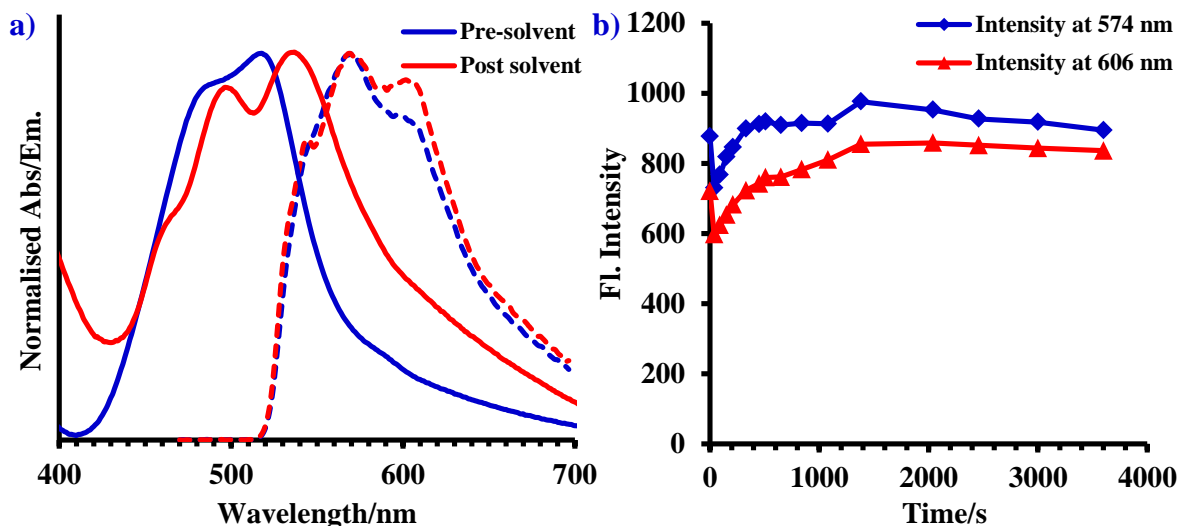
Figure S6.7. a) Normalised absorption (solid lines) and emission (dashed lines, excitation 450 nm with a 520 nm filter to reduce scattering effects) spectra for an **HBDPP** *as-deposited*, ordered thin film before (blue) and after (red) solvent annealing with **acetone** vapour. The change in absorption spectrum is consistent with enhanced crystallinity in the films after solvent treatment. b) Emission intensity as a function of time for the bands at 570 nm and 606 nm during **acetone** exposure. Of note is that the overall fluorescence emission is not quenched during solvent treatment with the increase in relative emission at 606 nm consistent with crystallisation of the thin film and formation of cofacial H-aggregates.
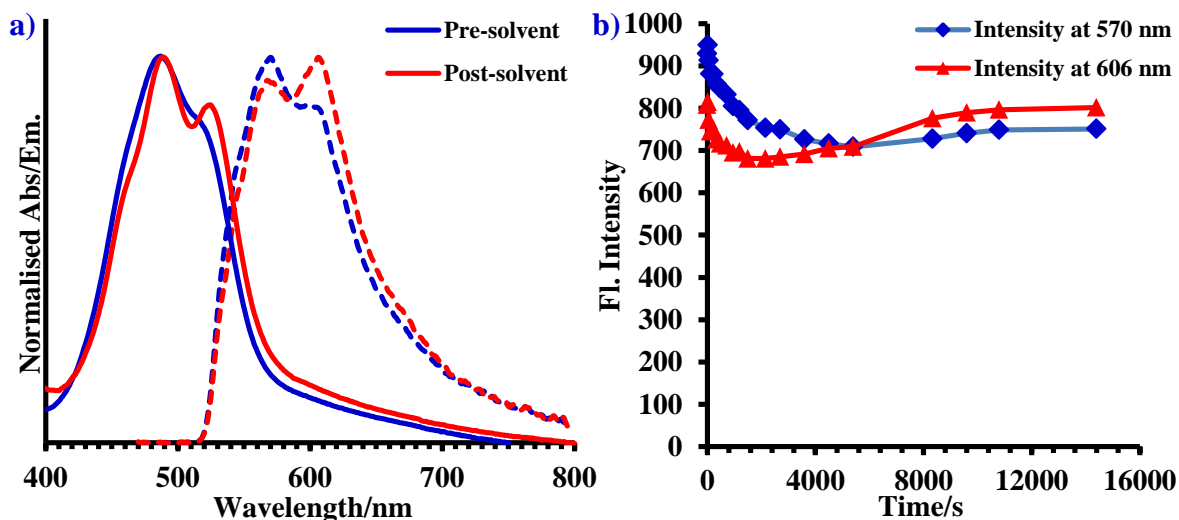
Figure S6.8. a) Normalised absorption (solid lines) and emission (dashed lines, excitation 450 nm with a 520 nm filter to reduce scattering effects) spectra for an **HBDPP** *as-deposited*, ordered thin film before (blue) and after (red) solvent annealing with **toluene** vapour. Enhanced vibronic structure in the absorption spectrum is consistent with enhanced crystallinity in the films after solvent treatment. b) Emission intensity as a function of time for the bands at 570 nm and 606 nm during **toluene** exposure. Again, the overall fluorescence emission is not quenched during solvent treatment with the increase in relative emission at 606 nm consistent with crystallisation of the thin film and formation of cofacial H-aggregates.

Table S6.2. Absorption (λ_{abs}) and fluorescence emission maxima (λ_{em}) for **HBDPP** solvent annealed spin-coated thin films on SiO_2 (* appears as a shoulder).

	Acetone	**Toluene**	**Nitrobenzene**
λ_{abs} **(nm)**	463*, 497, 537	463*, 489, 524	463*, 490, 527
λ_{em}**(nm)**	543*, 570, 606	543*, 570, 607	543*, 570, 606
E_{0-0} **(cm^{-1})**	17985	18382	18399
Stokes Shift (cm^{-1})	205	667	559

Transmission X-ray diffraction data collection from a powder sample of BBDPP:

A sample of **BBDPP** was lightly dispersed in an agate mortar and pestle, before being filled into a 0.7 mm borosilicate glass capillary and mounted and aligned on a Bruker-AXS D8 diffractometer. PXRD data were collected at *RT* over the range 3.5–33° 2θ (2 kW; Cu $K_{\alpha 1}$, 1.54056 Å; step size 0.017°; 3.2 s per step; LynxEye detector).

The *RT* monochromatic capillary transmission powder X-ray diffraction (PXRD) data for **BBDPP** were Pawley-fitted satisfactorily in the program TOPAS (3.5 – 33° 2θ), starting from *RT* monoclinic lattice parameters determined using DICVOL04 and space group $P2_1/n$ reported for the single-crystal (SX) structure of **BBDPP** determined at $T = 100$ K. Across the pattern, the fit to the data is good, yielding refined *RT* unit cell parameters that are consistent with the 100 K SX structure (see table below and **Figure S6.9**).

BBDPP data	*a* / Å	*b* / Å	*c* / Å	β / °	*V* / Å³
PXRD, *RT*	20.661(4)	5.3715(7)	20.778(7)	115.605(7)	2079.4(9)
SX, *T*=100 K	20.5116(14)	5.1146(4)	21.4898(15)	116.490(2)	2017.8(3)

Reflection XRD data collection from solvent-annealed films of BBDPP:

Solvent treatment of *as-deposited* ordered **BBDPP** thin films was carried out using the approach employed during solid state fluorescence quenching (SI.5), with nitroaromatic samples replaced by neat acetone or toluene. XRD patterns of **BBDPP** thin films treated with acetone or toluene on scattering SiO_2 substrates were collected at *RT* over the range of 5-40° 2θ using a Siemens D5000 diffractometer (Cu Kα, 40 kV/30 mA).
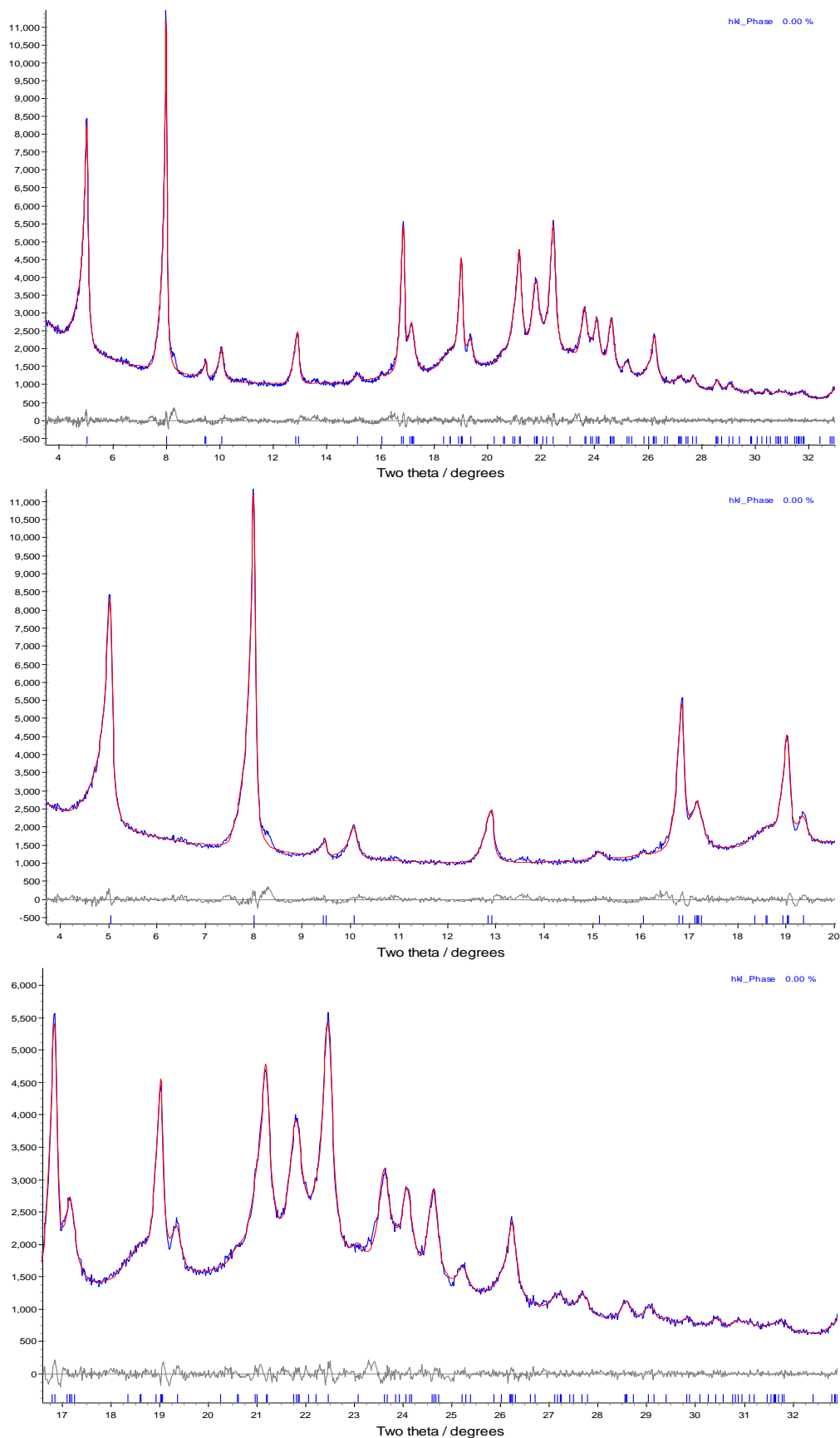
Figure S6.9. The result of a Pawley refinement using **BBDPP** unit cell parameters and *RT* PXRD data in the range 3.5 - 33° 2θ [R_{wp} = 3.51, zero point error = 0.012(2); **blue** = observed pattern, **red** = calculated profile (generated from the refinement), grey = difference between observed and calculated]. Tick marks along the bottom of the plot highlight the calculated reflection positions.
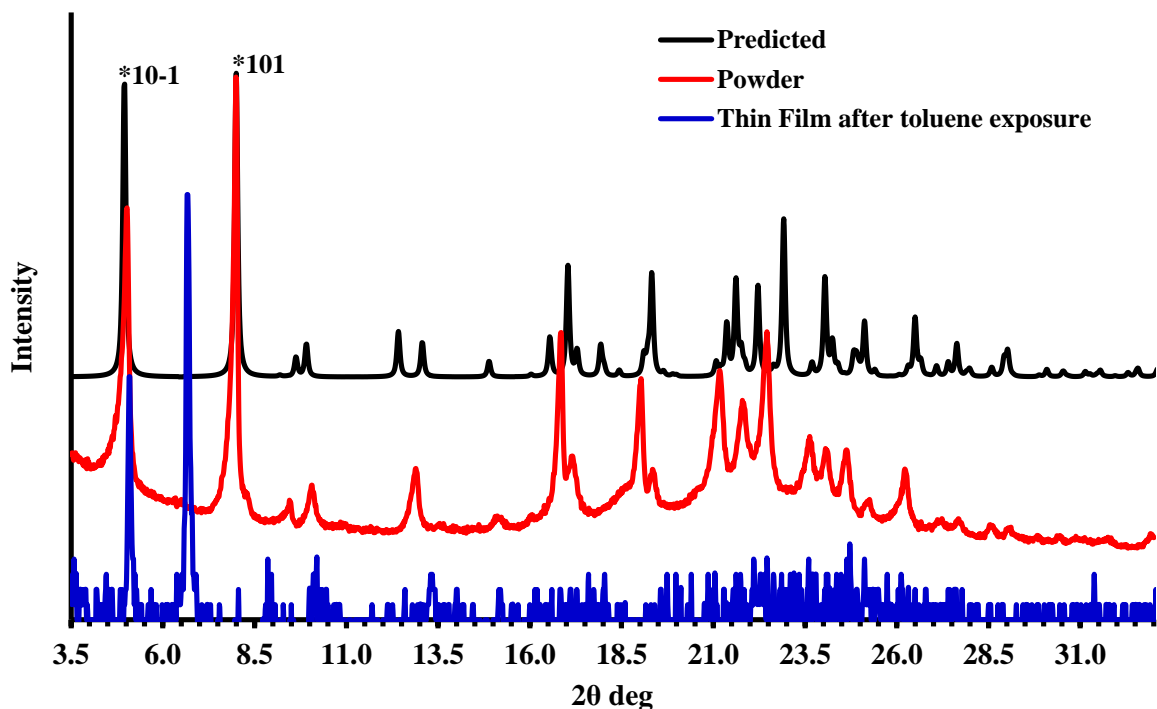
Figure S6.10. XRD patterns (offset for clarity) from **BBDPP** bulk powder (middle, red) and predicted XRD pattern determined in Mercury from single crystal X-ray structure (top, black) (most intense planes are indicated by *). The reflection geometry XRD pattern from a **toluene** annealed thin film of **BBDPP** on scattering SiO_2 substrate is also shown (blue, bottom and corrected for background substrate scatter) and is consistent with the proposed presence of a new crystal phase in the thin film environment (similar data obtained from an **acetone** annealed film).
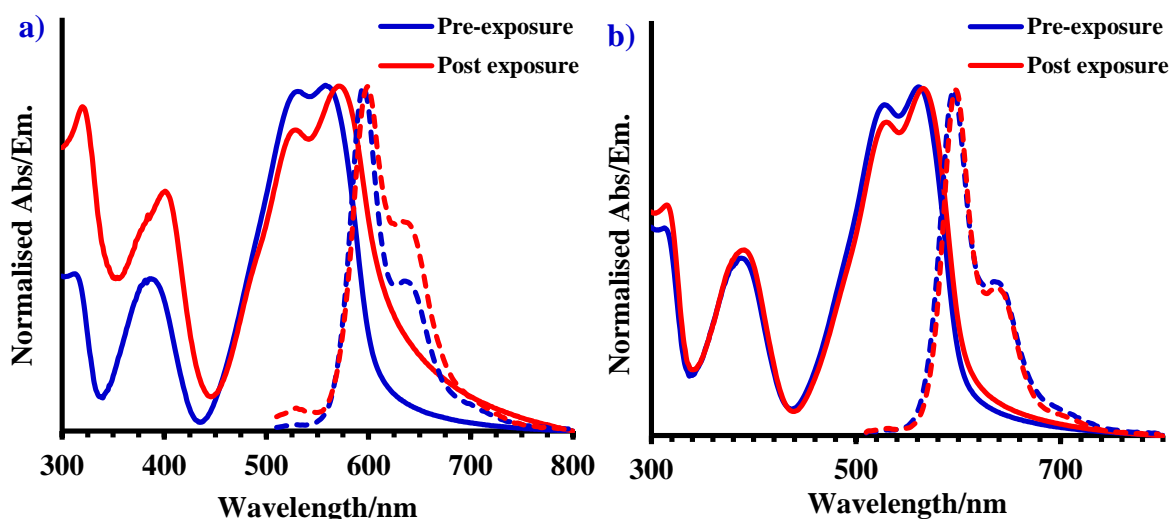

Figure S6.11. Normalised absorption (solid lines) and emission (dashed lines, excitation 540 nm) spectra for **BBDPP** *as-deposited*, ordered 400 nm thin films before (blue) and after (red) solvent annealing with a) **toluene** and b) **acetone** vapour.
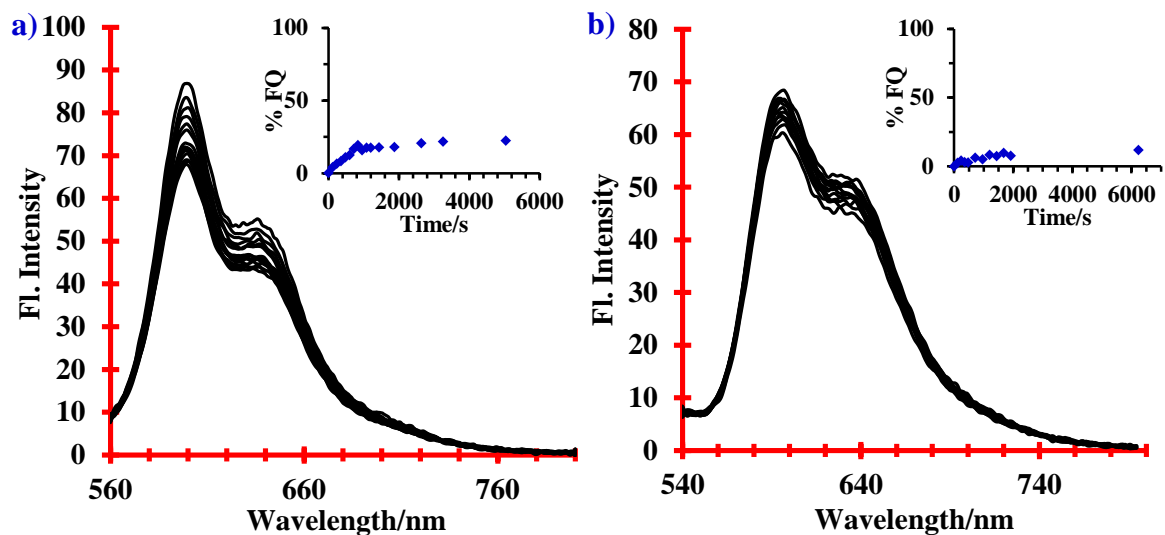
Figure S6.12. Emission spectra and inset showing fluorescence quenching as a function of time at 597 nm (Excitation at 540 nm) for a) 400 nm **BBDPP** toluene annealed thin film upon exposure to **DNT** vapour and b) 400 nm **BBDPP** acetone annealed thin film upon exposure to **NB**. In both cases a rapid rise to emission saturation is observed, consistent with the **BBDPP** *as-deposited* ordered thin film response; in the case of the solvent annealed films the lower overall emission quenching is due to a reduction in film surface area and accessibility of quenchable emissive sites.

References

1. J. Calvo, M. Warzecha, A. R. Kennedy, C. J. McHugh and A. J. McLean, *Cryst. Growth. Des*, 2014, 14, 4849.

2. J. Kuwabara, T. Yamagata and T. Kanbara, *Tetrahedron*, 66, 2010, 3736.

3. S. J. Cole & P. A. Gale, *Chem. Sci*., (2012), 3, 683.

4. G. M. Sheldrick, *Acta Crystallogr*., 2008, A64, 112.

5. U. Resch-Genger, D. Pfeifer, C. Monte, W. Pilz, A. Hoffmann, M. Spieles, K. Rurack, J. Hollandt, D. Taubert, B. Schonenberger and P. Nording, *Journal of Fluorescence* 2005, 15, 315.

6. C. A. Parker, and W. T. Rees, *Analyst*, 1960, 85, 14.

7. Y. Shao, L. F. Molnar, Y. Jung, J. Kussmann, C. Ochsenfeld, S. T. Brown, A. T. B. Gilbert, L. V. Slipchenko, S. V. Levchenko, D. P. O'Neill, R. A. DiStasio Jr., R. C. Lochan, T. Wang, G. J. O. Beran, N. A. Besley, J. M. Herbert, C. Y. Lin, T. Van Voorhis, S. H. Chien, A. Sodt, R. P. Steele, V. A. Rassolov, P. E. Maslen, P. P. Korambath, R. D. Adamson, B. Austin, J. Baker, E. F. C. Byrd, H. Dachsel, R. J. Doerksen, A. Dreuw, B. D. Dunietz, A. D. Dutoi, T. R. Furlani, S. R. Gwaltney, A. Heyden, S. Hirata, C.-P. Hsu, G. Kedziora, R. Z. Khalliulin, P. Klunzinger, A. M. Lee, M. S. Lee, W. Liang, I. Lotan, N. Nair, B. Peters, E. I. Proynov, P. A. Pieniazek, Y. M. Rhee, J. Ritchie, E. Rosta, C. D. Sherrill, A. C. Simmonett, J. E. Subotnik, H. L. Woodcock III, W. Zhang, A. T. Bell, A. K. Chakraborty, D. M. Chipman, F. J. Keil, A. Warshel, W. J. Hehre, H. F. Schaefer, III, J. Kong, A. I. Krylov, P. M. W. Gill and M. Head-Gordon, *Phys. Chem. Chem. Phys*., 2006, 8, 3172.

8. N. G. Tsierkezos, *J. Solution Chem*., 2007, 36, 289.

9. N. G. Tsierkezos, and U. J. Ritter, *Appl. Electrochem*., 2010, 40, 409.

10. R. R. Gagne, C. A. Koval, and G. C. Lisensky, *Inorganic Chemistry*, 1980, 19, 2854.

11. Y. Liu, M. S. Liu and A. K. Y. Jen, *Acta Polym*., 1999, 50, 105.

12. J. R. Lakowicz, *Principles of Fluorescence Spectroscopy*; 3rd ed.; Springer, 2006.

13. S. Nad, and H. Pal, *J. Phys. Chem. A.,* 2000, 104, 673.

14. S. S. Nagarkar, A. V. Desai and S. K. Ghosh, *Chem. Commun*., 2014, 50, 8915.

15. C. Vijayakumar, G. Tobin, W. Schmitt, M. J. Kim and M. Takeuchi, *Chem. Commun*., 2010, 46, 874.

16. N. Venkatramaiah, A. D. G. Firmino, F. A. A. Paz and J. P. C. Tome, *Chem. Commun*., 2014, 50, 9683.

17. J. L. Bredas, *Mater. Horiz.*, 2014, 1, 17.

18. J. Yang and T. M. Swager, *J. Am. Chem. Soc*., 1998, 120, 11864.

19. S. W. Thomas, G. D. Joly and T. M. Swager, *Chem. Rev*., 2007, 107, 1339.